Springer

Acta Mechanica Sinica

CrossMark click for updates

• RESEARCH PAPER •

Acta Mech. Sin., Vol. 41, 424445 (2025)
https://doi.org/10.1007/s10409-024-24445-x

Investigation of non-Schmid effects in dual-phase steels using a dislocation density-based crystal plasticity model

Jianchang Zhu[1], Mohamed Ben Bettaieb[2], Zhenhuan Li[1,3], Farid Abed-Meraim[2], and Minsheng Huang[1,3*]

[1] *Department of Mechanics, School of Aerospace Engineering, Huazhong University of Science and Technology, Wuhan 430074, China;*
[2] *LEM3, CNRS, Arts et Métiers Institute of Technology, Université de Lorraine, Metz F-57070, France;*
[3] *Hubei Key Laboratory of Engineering Structural Analysis and Safety Assessment, Wuhan 430074, China*

Received September 4, 2024; accepted October 14, 2024; published online March 5, 2025

Non-Schmid (NS) effects in body-centered cubic (BCC) single-phase metals have received special attention in recent years. However, a deep understanding of these effects in the BCC phase of dual-phase (DP) steels has not yet been reached. This study explores the NS effects in ferrite-martensite DP steels, where the ferrite phase has a BCC crystallographic structure and exhibits NS effects. The influences of NS stress components on the mechanical response of DP steels are studied, including stress/strain partitioning, plastic flow, and yield surface. To this end, the mechanical behavior of the two phases is described by dislocation density-based crystal plasticity constitutive models, with the NS effect only incorporated into the ferrite phase modeling. The NS stress contribution is revealed for two types of microstructures commonly observed in DP steels: equiaxed phases with random grain orientations, and elongated phases with preferred grain orientations. Our results show that, in the case of a microstructure with equiaxed phases, the normal NS stress components play significant roles in tension-compression asymmetry. By contrast, in microstructures with elongated phases, a combined influence of crystallographic texture and NS effect is evident. These findings advance our knowledge of the intricate interplay between microstructural features and NS effects and help to elucidate the mechanisms underlying anisotropic-asymmetric plastic behavior of DP steels.

DP steels, Non-Schmid effects, Crystal plasticity modeling, Tension-compression asymmetry

Citation: J. Zhu, M. B. Bettaieb, Z. Li, F. Abed-Meraim, and M. Huang, Investigation of non-Schmid effects in dual-phase steels using a dislocation density-based crystal plasticity model, Acta Mech. Sin. 41, 424445 (2025), https://doi.org/10.1007/s10409-024-24445-x

1. Introduction

As typical advanced high-strength steels, ferrite-martensite dual-phase (DP) steels have gained widespread use in multiple applications, particularly in the automotive industry. Their use allows weight reduction and enhances crash performance of industrial components. This steel category can be seen as a composite of ferrite and martensite phases. The former has a body-centered cubic (BCC) crystallographic structure, while the latter presents a body-centered tetragonal structure. The inherent properties of the ferrite and martensite phases, with the former being soft and ductile and the latter being hard and brittle, enable to produce DP steels with an optimized ductility/strength ratio through thoughtful microstructure design. More importantly, thorough understanding of the intricate relationships between microstructure and macroscopic properties is crucial for the design of new DP steels. Tailoring microstructural features, such as martensite volume fraction (MVF), morphology, hardness, grain size, and orientation, offers the potential to obtain optimized DP steels with a variety of mechanical properties in terms of yield strength, tensile strength, and forming limit strain. In this field, some studies have explored the impact of microstructural features, particularly the MVF and morphology. Notably, an increase in MVF results in higher yield and tensile strength, but a reduced uniform elongation of DP steels [1,2]. The phase

*Corresponding author. E-mail address: mshuang@hust.edu.cn (Minsheng Huang)
Executive Editor: Huiling Duan

morphology also significantly impacts the mechanical behavior for a given composition and phase volume fraction. As demonstrated by Pierman et al. [3], equiaxed microstructures lead to higher strength and lower ductility, as compared to dispersed elongated microstructures. Further details regarding the effect of martensite morphology can be found in Ref. [1], where the studied morphological parameters include the aspect ratio of martensite phase, the combination of various aspect ratios, and the interconnectivity between martensite phase and its thickness. Additionally, the martensite hardness, which is determined by the carbon content in the martensitic phase, affects the overall mechanical properties and plastic behavior of DP steels. It has been demonstrated that the martensite hardness has a limited influence on the initial yield strength, becoming significant only when the MVF is relatively large [2]. Besides, the martensite island size is supposed to be an influential factor in the mechanical behavior of DP steels. To assess this, Basu et al. [4] investigated the variation of effective stress, strain, triaxiality distribution, and partitioning in two phases with varying the martensite island size, thus demonstrating a limited influence of the martensite island size [4]. Using the same strategy, Basu et al. [4] highlighted the significant impacts of the MVF and phase strength contrast. The phase strength contrast, together with phase distribution, can dictate the plastic activity of DP steels, as revealed in Ref. [5]. Another important factor in the mechanical behavior of DP steels is the initial grain orientation in the ferrite phase [6,7]. The associated mechanism has been interpreted by Jafari et al. [7] from the dislocation density perspective: the initial grain orientation affects the stored dislocation density within ferrite grains and, consequently, the energy absorption capacity of DP steels, which eventually impacts the plasticity, the evolution of shear bands, and thus the ductility [7].

The aforementioned investigations enhance our understanding of the microstructure-macroscopic property relationships in DP steels. Nevertheless, to guide the optimization of DP steels, a micromechanical constitutive model explicitly accounting for the microstructural features is required. For the simulations of DP steels, three prevalent constitutive strategies are often adopted: (I) phenomenological models for both phases, (II) a crystal plasticity model for the ferrite phase and a phenomenological model for the martensite phase, and (III) crystal plasticity models for both phases. Using the first strategy, there have been many contributions devoted to gaining insights into the mechanical behavior of DP steels [1-3,5,8-12]. To capture the microstructural effects within the first strategy, one needs to introduce several internal parameters representing the microstructural features (e.g., the parameter representing the carbon content to quantify the influence of martensitic hardness, see Ref. [2]), or to adopt multiscale simulations (e.g., two-level simulations by Matsuno et al. [12], Mori-Tanaka based homogenization model by Pierman et al. [3]). Other homogenization models for DP steels can also be found in the literature, such as the enhanced homogenization anisotropic model [13,14], or the mean-field composite model [15,16]. The investigations using the second strategy [7,17-19] generally assume that the specific response of martensite phase is not that important to the mechanical response of DP steels, as the martensite phases undergo significantly smaller plastic deformation, as compared to the ferrite phases. However, Ref. [20] demonstrated the importance of the specific response of martensite (plasticity and damage) in DP600 steel. This in turn underlines some of the major drawbacks of the second strategy. The third strategy employs crystal plasticity models for both phases, thus providing a more detailed picture of stress and strain partitioning and enabling a more physically-based consideration of microstructural effects, such as the local heterogeneity in individual phases. Moreover, the third strategy allows obtaining the constitutive parameters for each phase by calibrating with microscale experiments, such as micropillar compression tests. In such a way, the constitutive models are supposed to be microscale-calibrated [21-23], which should enable rationalizing the experimental findings.

Although various series of DP steels are widely used in the industry, their macroscopic behavior and the associated microscopic mechanisms are still not fully understood. More recently, some researchers have paid attention to the anisotropy-asymmetry behavior (i.e., anisotropic and tension-compression (T-C) asymmetric) of several DP steels. In this field, Hou et al. [24] have used a series of mechanical tests to reveal the anisotropic yield behavior of DP590, DP780, and DP980 steels. Maeda et al. [25] have conducted an in-plane uniaxial tension/compression test to validate the T-C asymmetry of flow stress for DP980 steel. Mehrabi et al. [26] and Noma and Kuwabara [27] have used bending tests to investigate the T-C asymmetry of DP980 and DP780 steels. These contributions have confirmed that the anisotropic yield behavior and the T-C asymmetry cannot be neglected when characterizing the mechanical behavior of DP steels. To model these effects, some phenomenological anisotropic-asymmetric yield functions [28-32] have recently been proposed. These models accurately describe the anisotropy-asymmetry phenomenon, but cannot account for the microstructural features that can be naturally considered by crystal plasticity models. Based on the works in Refs. [22,23,33], it is speculated that the anisotropy-asymmetry properties of DP steels are closely related to the non-Schmid (NS) behavior of the ferrite phase. The NS behavior, known to violate the Schmid law, is commonly observed in BCC single crystals but remains elusive in DP steels. Inspired by this, the present paper adopts microscale-calibrated crystal plasticity models for both phases to probe the NS effects on

the mechanical response of DP steels. To this end, dislocation density-based crystal plasticity models (incorporating NS effects for the ferrite phase, without NS effects for the martensite phase) are calibrated and implemented to describe the mechanical behavior of DP steels.

The remainder of this paper is arranged as follows: Sect. 2 details the computational modeling, including the microstructures of the studied DP steels, the crystal plasticity models for the two phases, as well as the boundary conditions and loadings; Sect. 3 presents the results and discusses the NS effects on the mechanical responses; Sect. 4 ends the paper with some conclusions.

2. Computational modeling

2.1 Microstructures and finite element modeling

Two microstructures of DP steel sheets are considered in this paper: a microstructure with equiaxed phases (hereafter referred to as equiaxed microstructure, unless otherwise stated) and a microstructure with elongated phases (hereafter designated as elongated microstructure, unless otherwise stated). The microstructures are represented by three-dimensional Voronoi tessellation-based representative volume elements (RVEs), generated using DREAM3D software [34]. The size of the RVEs is taken to be dimensionless 1×1×0.1. For the equiaxed microstructure, the phases are initially equiaxed and randomly distributed (as shown in Fig. 1(a)), with both the ferrite and martensite grains being randomly oriented (as depicted in Fig. 2(a) on the pole figure). For the elongated microstructure, the phases are initially elongated in the first direction (as shown in Fig. 1(b)), with both the ferrite and martensite grains having orientations associated with pronounced crystallographic textures (as illustrated in Fig. 2(b) on the pole figure, which displays a typical rolling texture). The two types of DP steel microstructures can be commonly observed by microscopy analysis [1] and are produced through heat treatments [35,36]. Both of the RVEs are composed of 403 grains (as illustrated in Fig. 1(c) and (d), which depict the grain morphologies), and are discretized by 21600 (60×60×6) eight-node hexahedral elements. The grain number and finite element number are sufficient to reach an accurate mechanical response using finite element computations, as supported by the analyses in Refs. [37-39]. The number of martensite particles contained in the RVEs is also sufficient

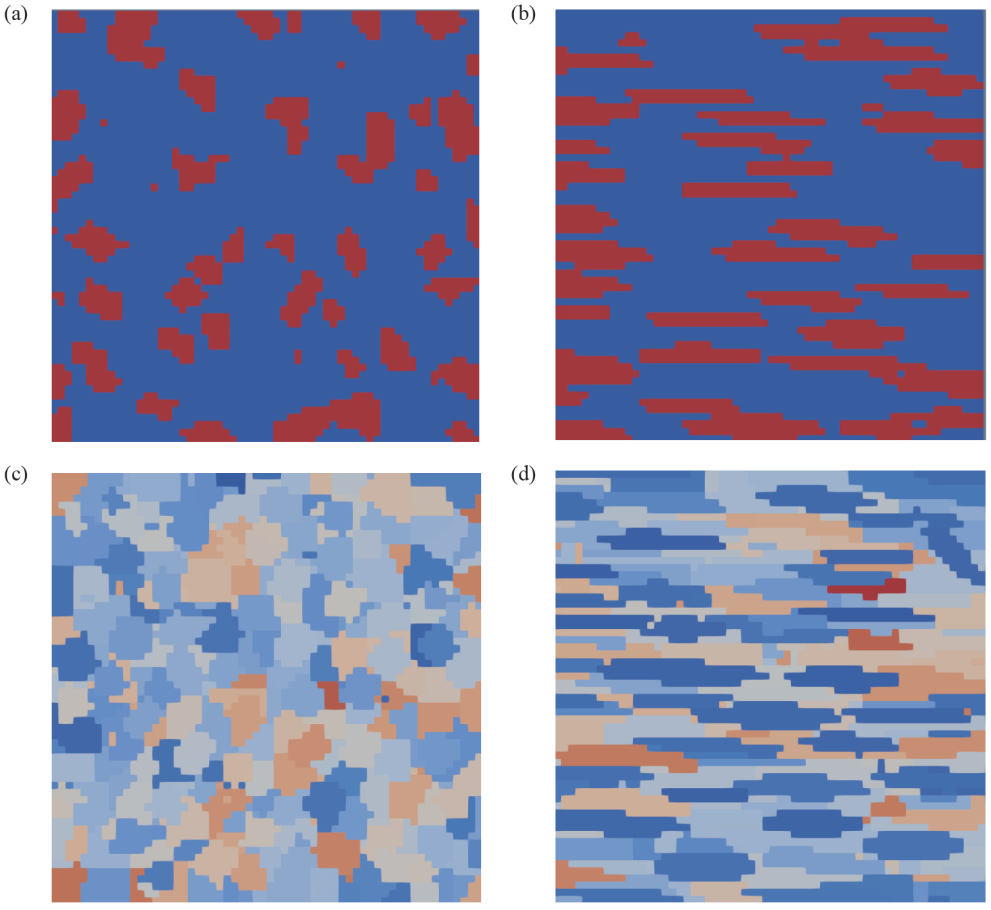

Figure 1 Phase morphology: (a) equiaxed phases and (b) elongated phases, ferrite and martensite phases are respectively marked by blue and red color; the grain morphology: (c) equiaxed phases and (d) elongated phases.

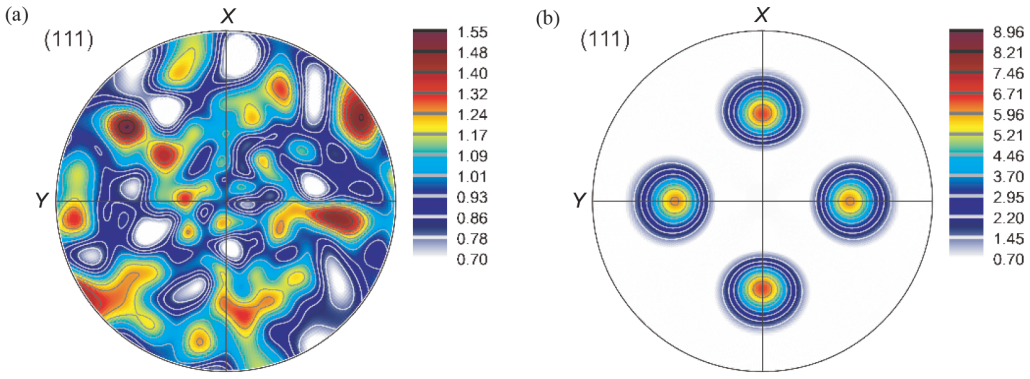

Figure 2 (111) pole figures of (a) equiaxed microstructure and (b) elongated microstructure.

for the simulations of DP steels. The grain size effect is not involved in this study since it is not our concern.

2.2 Crystal plasticity model with NS effect

2.2.1 Constitutive model

The mechanical behavior of both the ferrite and martensite phases is modeled using a dislocation density-based crystal plasticity approach. For the ferrite phase, a dislocation density-based constitutive model accounting for the NS effect is used. This effect violates the classical Schmid law and is commonly observed in BCC crystals [40]. For the martensite phase, a dislocation density-based hardening law is also adopted, but NS effects are not considered, in the same way as in Refs. [22,23].

The crystal plasticity models used in this study follow a rate-independent framework. The elastic behavior of the single crystals is described by a hypoelastic law, which states that the lattice corotational rate $\boldsymbol{\sigma}^{\nabla}$ of the Cauchy stress tensor $\boldsymbol{\sigma}$ is related to the elastic strain rate $\mathbf{d}_e$ by the fourth-order elasticity tensor $\mathbf{C}_e$

$$\boldsymbol{\sigma}^{\nabla} = \dot{\boldsymbol{\sigma}} - \mathbf{w}_e \cdot \boldsymbol{\sigma} + \boldsymbol{\sigma} \cdot \mathbf{w}_e = \mathbf{C}_e : \mathbf{d}_e, \tag{1}$$

where $\dot{\boldsymbol{\sigma}}$ is the time derivative of the Cauchy stress tensor $\boldsymbol{\sigma}$, and $\mathbf{w}_e$ is the elastic part of the spin tensor $\mathbf{w}$. The elastic properties are different for the ferrite and martensite phases. More specifically, for the ferrite phase, the elastic properties are assumed to have cubic symmetry [23]. As to the martensite phase, the elastic properties are assumed to be isotropic [23]. The values of the elasticity constants for both phases are taken from Ref. [23].

The plastic flow in this study is modeled assuming that plastic deformation is only due to the mechanism of shear slip. Thus, the plastic strain rate and plastic spin tensors $\mathbf{d}_p$ and $\mathbf{w}_p$ take the following expressions:

$$\mathbf{d}_p = \sum_{\alpha=1}^{N_s} \dot{\gamma}^{\alpha} \mathbf{R}^{\alpha}, \quad \mathbf{w}_p = \sum_{\alpha=1}^{N_s} \dot{\gamma}^{\alpha} \mathbf{S}^{\alpha}, \tag{2}$$

where $\dot{\gamma}^{\alpha}$ is the slip rate on the α-th slip system, and N_s refers to the total number of slip systems. In this study, N_s is equal to 24 for both phases. For the ferrite phase, the full set of 24-$\{110\}\langle 111\rangle$ slip systems is used [23,41] (see Table A1). As to the martensite phase, the standard slip systems of 12-$\{110\}\langle 111\rangle$ and 12-$\{112\}\langle 111\rangle$ are considered [23] (see Table A2). $\mathbf{R}^{\alpha}$ (resp. $\mathbf{S}^{\alpha}$) is the symmetric part (resp. skew-symmetric part) of the classical Schmid tensor $\mathbf{M}^{\alpha}$, which is itself equal to the tensor product of slip direction vector $\vec{\mathbf{m}}^{\alpha}$ and the normal vector to slip plane $\vec{\mathbf{n}}^{\alpha}$

$$\forall\ \alpha = 1,\ ...,\ N_s:\ \mathbf{M}^{\alpha} = \vec{\mathbf{m}}^{\alpha} \otimes \vec{\mathbf{n}}^{\alpha}. \tag{3}$$

Within the framework considering the NS effects, the plastic flow is governed by a generalized Schmid law, stating that a slip system becomes activated only when the resolved shear stress τ_*^{α} reaches a critical value τ_c^{α}

$$\forall\ \alpha = 1, ..., N_s: \quad \begin{cases} \tau_*^{\alpha} < \tau_c^{\alpha} \Rightarrow \dot{\gamma}^{\alpha} = 0, \\ \tau_*^{\alpha} = \tau_c^{\alpha} \Rightarrow \dot{\gamma}^{\alpha} \geq 0, \end{cases} \tag{4}$$

where τ_*^{α} is defined in terms of $\boldsymbol{\sigma}$ and $\mathbf{R}_*^{\alpha}$ as follows:

$$\forall\ \alpha = 1, ..., N_s:\ \tau_*^{\alpha} = \boldsymbol{\sigma} : \mathbf{R}_*^{\alpha}. \tag{5}$$

With the NS effect included, $\mathbf{R}_*^{\alpha}$ is the symmetric part of the generalized Schmid tensor $\mathbf{M}_*^{\alpha}$, which is provided by

$$\mathbf{M}_*^{\alpha} = \mathbf{M}^{\alpha} + \mathbf{M}_{\mathrm{NS}}^{\alpha}, \tag{6}$$

where $\mathbf{M}^{\alpha}$ is defined by Eq. (3), while $\mathbf{M}_{\mathrm{NS}}^{\alpha}$ is the NS tensor given by a five-term formulation [42,43]

$$\begin{aligned} \mathbf{M}_{\mathrm{NS}}^{\alpha} &= c_1 \mathbf{M}_{\mathrm{NS}}^{\alpha,tm} + c_2 \mathbf{M}_{\mathrm{NS}}^{\alpha,tn} + c_3 \mathbf{M}_{\mathrm{NS}}^{\alpha,nn} + c_4 \mathbf{M}_{\mathrm{NS}}^{\alpha,tt} + c_5 \mathbf{M}_{\mathrm{NS}}^{\alpha,mm} \\ &= c_1 \vec{\mathbf{t}}^{\alpha} \otimes \vec{\mathbf{m}}^{\alpha} + c_2 \vec{\mathbf{t}}^{\alpha} \otimes \vec{\mathbf{n}}^{\alpha} + c_3 \vec{\mathbf{n}}^{\alpha} \otimes \vec{\mathbf{n}}^{\alpha} + c_4 \vec{\mathbf{t}}^{\alpha} \otimes \vec{\mathbf{t}}^{\alpha} \\ &\quad + c_5 \vec{\mathbf{m}}^{\alpha} \otimes \vec{\mathbf{m}}^{\alpha}. \end{aligned} \tag{7}$$

In Eq. (7), $\vec{\mathbf{t}}^{\alpha}$ is a unit vector tangent to the α-th slip system, such that $\vec{\mathbf{t}}^{\alpha} = \vec{\mathbf{m}}^{\alpha} \times \vec{\mathbf{n}}^{\alpha}$. c_1-c_5 are weighting coefficients, which determine the effects of each NS stress component. It is noted that only four of these coefficients (i.e., c_1-c_4) are independent when the yield is assumed to be independent of hydrostatic stresses. In this case, c_5 is taken to be $-(c_3 + c_4)$ [42,44]. The values of NS coefficients c_i can be

obtained by either single crystal experiments [42], or atomistic simulations [45].

The critical shear stress τ_c^α is determined by a dislocation density-based formulation, which accounts for the dislocation interactions in relation to their nucleation, storage, and annihilation [46]

$$\tau_c^\alpha = \tau_0^\alpha + sGb\sqrt{\sum_{\beta=1}^{N_s} a_{\alpha\beta}\rho^\beta}, \tag{8}$$

where τ_0^α is the initial critical shear stress, s is a constant related to the stability of dislocation configuration, G is the shear modulus, b is the magnitude of the Burgers vector, and $a_{\alpha\beta}$ is the $\alpha\beta$ component of the anisotropy interaction matrix [47]. The dislocation density ρ^α evolves according to [48]

$$\dot{\rho}^\alpha = \dot{\gamma}^\alpha\left(\frac{1}{bk_a}\sqrt{\sum_{\beta\neq\alpha}^{N_s}\rho^\beta} - \frac{k_b}{b}\rho^\alpha\right), \tag{9}$$

where k_a is a parameter related to dislocation storage, and k_b is the critical annihilation distance of dislocations. The involved five constitutive parameters, including the initial dislocation density ρ_0, can be determined by experiments.

In the present study, the NS tensor $\mathbf{M}_{\mathrm{NS}}^\alpha$ is introduced as a correction tensor for the ferrite phase in order to account for the NS behavior. It is assumed that the martensite phase does not exhibit NS behavior. Accordingly, $\mathbf{M}_{\mathrm{NS}}^\alpha$ is omitted for the martensite phase, whose constitutive modeling reduces to the formulation based on the classical Schmid law.

2.2.2 *Numerical aspects of NS constitutive model*

The constitutive model is implemented via user-defined material subroutine within ABAQUS [49]. The constitutive equations are iteratively solved using an ultimate numerical algorithm (detailed in Refs. [47,50,51]). In this subsection, the rate forms of some equations are briefly presented to highlight the main particularities induced by the presence of NS terms.

The time derivative of τ_*^α (defined by Eq. (5)) is calculated as

$$\forall\ \alpha = 1,\ ...,\ N_s:\ \dot{\tau}_*^\alpha = \boldsymbol{\sigma}^\nabla : \mathbf{R}_*^\alpha. \tag{10}$$

Combining Eqs. (1) and $(2)_1$, the co-rotational stress rate $\boldsymbol{\sigma}^\nabla$ can be obtained as

$$\boldsymbol{\sigma}^\nabla = \mathbf{C}_e : \mathbf{d} - \sum_{\alpha=1}^{N_s}\dot{\gamma}^\alpha \mathbf{C}_e : \mathbf{R}^\alpha. \tag{11}$$

Using Eq. (11), Eq. (10) is rewritten as

$$\forall\ \alpha = 1,\ ...,\ N_s:$$

$$\dot{\tau}_*^\alpha = \mathbf{R}_*^\alpha : (\mathbf{C}_e : \mathbf{d}) - \sum_{\beta=1}^{N_s}\dot{\gamma}^\beta \mathbf{R}_*^\alpha : \mathbf{C}_e : \mathbf{R}^\beta. \tag{12}$$

According to Eq. (4), the set of active slip systems $\mathcal{A}$ is determined by

$$\forall\,\alpha\in\mathcal{A}:\quad \dot{\gamma}^\alpha > 0,\quad \dot{\tau}_*^\alpha - \dot{\tau}_c^\alpha = 0. \tag{13}$$

The critical shear stress rate $\dot{\tau}_c^\alpha$ in the generalized Schmid law evolves with the slip accumulation on the crystallographic slip systems as follows:

$$\forall\ \alpha = 1,\ ...,\ N_s:\quad \dot{\tau}_c^\alpha = \sum_{\beta=1}^{N_s} H^{\alpha\beta}\dot{\gamma}^\beta, \tag{14}$$

where $H^{\alpha\beta}$ is the $\alpha\beta$ component of the hardening interaction matrix $\mathbf{H}$. This interaction matrix, determined by differentiating Eq. (8) in combination with Eq. (9), can then be expressed as

$$\forall\ \alpha,\beta = 1,\ ...,\ N_s:$$

$$H^{\alpha\beta} = \frac{sG}{2\sqrt{\sum_{k=1}^{N_s} a^{\alpha k}\rho^k}}a^{\alpha\beta}\left(\frac{1}{k_a}\sqrt{\sum_{k\neq\beta}^{N_s}\rho^k} - k_b\rho^\beta\right). \tag{15}$$

Using Eqs. (12) and (14), Eq. (13) can be transformed as follows:

$$\forall\,\alpha\in\mathcal{A}:$$

$$\mathbf{R}_*^\alpha : (\mathbf{C}_e : \mathbf{d}) - \sum_{\beta\in\mathcal{A}}\left(\mathbf{R}_*^\alpha : \mathbf{C}_e : \mathbf{R}^\beta + H^{\alpha\beta}\right)\dot{\gamma}^\beta = 0. \tag{16}$$

Then, the slip rates of the active slip systems can be obtained by solving Eq. (16)

$$\forall\,\alpha\in\mathcal{A}:\quad \dot{\gamma}^\alpha = \sum_{\beta\in\mathcal{A}} Q^{\alpha\beta}\mathbf{R}_*^\beta : (\mathbf{C}_e : \mathbf{d}), \tag{17}$$

where $\mathbf{Q}$ is the inverse of matrix $\mathbf{P}$ defined by the following index form:

$$\forall\,\alpha,\beta\in\mathcal{A}:\quad P^{\alpha\beta} = \mathbf{R}_*^\alpha : \mathbf{C}_e : \mathbf{R}^\beta + H^{\alpha\beta}. \tag{18}$$

Recasting Eqs. (2) and (17) into the form of Eq. (1), the tangent modulus $\mathbf{C}_{ep}$ required in the numerical algorithm for finite element computations incorporating the NS effects can be determined as follows:

$$\mathbf{C}_{ep} = \mathbf{C}_e - \sum_{\alpha\in\mathcal{A}}\sum_{\beta\in\mathcal{A}} Q^{\alpha\beta}\left(\mathbf{C}_e : \mathbf{R}^\alpha + \mathbf{S}^\alpha\cdot\boldsymbol{\sigma} - \boldsymbol{\sigma}\cdot\mathbf{S}^\alpha\right) \otimes\left(\mathbf{R}_*^\beta : \mathbf{C}_e\right). \tag{19}$$

Additionally, analyzing Eqs. $(2)_1$ and (5), one can observe that

$$\mathbf{d}_p \neq \sum_{\alpha=1}^{N_s}\dot{\gamma}^\alpha\frac{\partial\tau_*^\alpha}{\partial\boldsymbol{\sigma}}. \tag{20}$$

This implies that the plastic flow at the single crystal scale

is non-associative with the yield criterion since stress components other than the Schmid stress contribute to the yield criterion. This subsection should be regarded as a concise overview of the numerical aspects with the NS terms involved in the constitutive equations.

2.2.3 *Identification of constitutive parameters*

The constitutive parameters of the ferrite and martensite phases are identified separately. The von Mises equivalent stress-strain curves obtained from crystal plasticity simulations of micropillar compression tests are fitted with the experimental data of DP980 steel taken from Ref. [22]. The boundary conditions and model setting in this fitting process, which closely follows Ref. [22], are described in more detail in Appendix B. For the ferrite phase, a [324]-oriented single-crystal micropillar is used to conduct the fitting process. [205] and [326]-oriented single-crystal micropillars are used to validate the set of parameters obtained in the fitting process. In this manner, an appropriate set of constitutive parameters is determined for the ferrite phase (see Fig. 3(a)). For the martensite phase, which is itself a hierarchical microstructure [52], the simulation of compression test of micropillar with multiple martensite blocks is conducted. The corresponding von Mises equivalent stress-strain curve is fitted to the experimental data (see Fig. 3(b)). The identified constitutive parameters for both phases are listed in Table 1. Following the work of Mapar et al. [53] on DP980 steel and the work of Patra et al. [54] on BCC Fe, as well as the study of Lim et al. [42], the NS coefficients are considered to take the following values for the ferrite of DP steel in the present study: $c_1 = 0.025$, $c_2 = -0.0227$, $c_3 = 0.1299$, $c_4 = -0.1299$, and $c_5 = 0$. With the material parameters and NS coefficients listed in Table 1, the overall tension and compression stress-strain curves of DP steel (equiaxed microstructure) with martensite volume fraction $MVF = 57\%$ are plotted in Fig. 4. It can be seen from this figure that the flow stress in uniaxial compression is ~5.5% higher than that in uniaxial tension. This is consistent with the experiments on DP980 steel conducted by Maeda et al. [25,55] (see Fig. 3(a) in Ref. [25]). The experimental data in Ref. [25] (represented in Fig. 4 for comparison purpose) show that the flow stress in compression is larger than that in tension by 6.2%, which is comparable to the data obtained by our simulation. This consistency validates that our NS crystal plasticity model is capable of accounting for the T-C asymmetry effects in DP steel. Therefore, the values of NS coefficients listed in Table 1 are adopted to account for the NS effects of DP steel in this study.

2.2.4 *Boundary conditions and macroscopic loadings*

In all the following computations of this study, the RVEs of DP steels are subjected to periodic boundary conditions

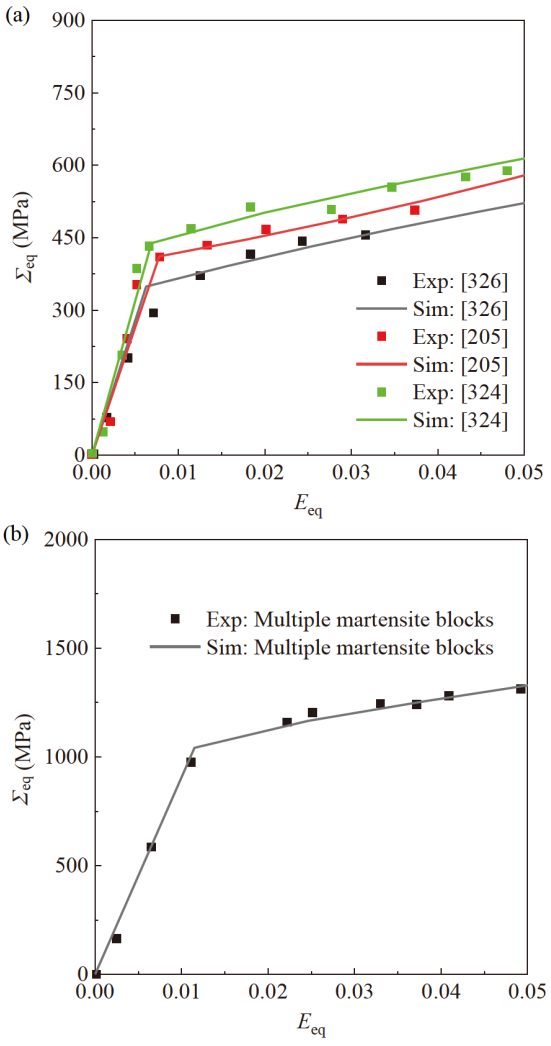

Figure 3 Fitting with the experimental data from Ref. [22]: (a) ferrite phase; (b) martensite phase.

(PBCs). Specifically, the PBCs are applied to the face pairs (B_1^+, B_1^-) and (B_2^+, B_2^-) of the RVEs (see Fig. 5 for the finite element discretization) via node-to-node constraints. The faces normal to the thickness direction are left unconstrained. For the sake of explanation, it is assumed that (M^+, M^-) denotes a node pair belonging to the face pairs (B_1^+, B_1^-) or (B_2^+, B_2^-). The PBCs require that the current positions of M^+ and M^- are related to their initial positions according to

$$\mathbf{x}_{M^-} = \mathbf{F}\cdot\mathbf{x}_{0M^-} + \mathbf{u}^{\mathrm{per}}_{M^-}, \quad \mathbf{x}_{M^+} = \mathbf{F}\cdot\mathbf{x}_{0M^+} + \mathbf{u}^{\mathrm{per}}_{M^+}, \tag{21}$$

where $\mathbf{x}$ and $\mathbf{x}_0$ denote the current and initial positions of the considered node pair, respectively, $\mathbf{F}$ is the deformation gradient, and $\mathbf{u}^{\mathrm{per}}$ is a periodic displacement field. Since the application of PBCs leads to $\mathbf{u}^{\mathrm{per}}_{M^+} = \mathbf{u}^{\mathrm{per}}_{M^-}$ for node pair (M^+, M^-), Eq. (21) is equivalent to the following form:

$$\mathbf{x}_{M^+} - \mathbf{x}_{M^-} = \mathbf{F}\cdot(\mathbf{x}_{0M^+} - \mathbf{x}_{0M^-}). \tag{22}$$

Table 1 Crystal plasticity constitutive model parameters used for DP steels in this study

Ferrite phase	Value	Source
Elasticity tensor component C_e^{1111} (GPa)	310	[23]
Elasticity tensor component C_e^{1122} (GPa)	145	[23]
Elasticity tensor component C_e^{1212} (GPa)	105	[23]
Initial critical shear stress τ_0 (MPa)	200	Fitted
Constant s	0.35	[56]
Shear modulus $G\left(=\sqrt{C_e^{1212}(C_e^{1111}-C_e^{1122})/2}\right)$ (GPa)	93.072	[23]
Dislocation storage parameter k_a	10	[57]
Critical annihilation distance of dislocations k_b (mm)	1.86×10^{-6}	Fitted
Burgers vector magnitude b (mm)	2.86×10^{-7}	[58]
Initial dislocation density ρ_0 (mm^{-2})	1×10^{8}	[58]
Non-Schmid coefficient c_1	0.025	[42,53]
Non-Schmid coefficient c_2	−0.0227	[42,53]
Non-Schmid coefficient c_3	0.1299	[42,53]
Non-Schmid coefficient c_4	−0.1299	[42,53]
Non-Schmid coefficient c_5	0	[42,53]
Martensite phase	**Value**	**Source**
Young's modulus E (GPa)	195	[23]
Poisson's ratio ν	0.3	[23]
Initial critical shear stress τ_0 (MPa)	520	Fitted
Shear modulus G $(=E/[2(1+\nu)])$ (GPa)	75	[22,23]
Dislocation storage parameter k_a	73	[22,23]
Critical annihilation distance of dislocations k_b (mm)	1×10^{-6}	Fitted
Burgers vector magnitude b (mm)	3×10^{-7}	[22,23]
Initial dislocation density ρ_0 (mm^{-2})	3×10^{7}	[22,23]

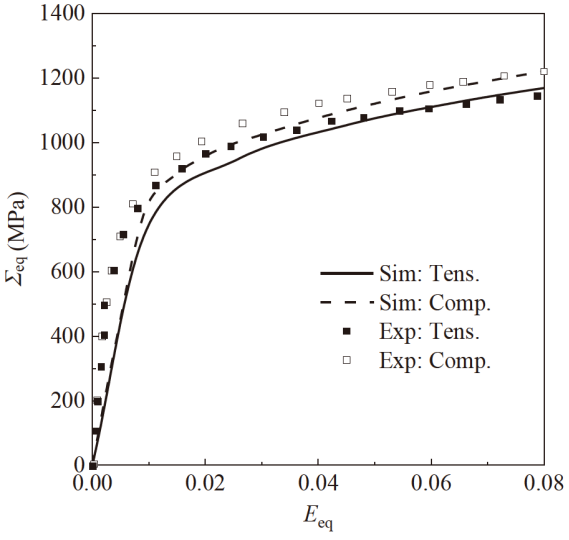

Figure 4 Tension-compression asymmetry of overall flow stress of DP980 steel obtained by NS crystal plasticity model and compared with experimental data from Refs. [25,55].

The displacement difference of nodes (M^+, M^-) is then expressed as

$$\mathbf{u}_{M^+}-\mathbf{u}_{M^-}=(\mathbf{F}-\mathbf{I})\cdot(\mathbf{x}_{0M^+}-\mathbf{x}_{0M^-}). \tag{23}$$

The details on the numerical implementation of Eq. (23) can be found in Refs. [59,60]. Equation (23) has to be enforced in the subsequent simulations carried out in this paper.

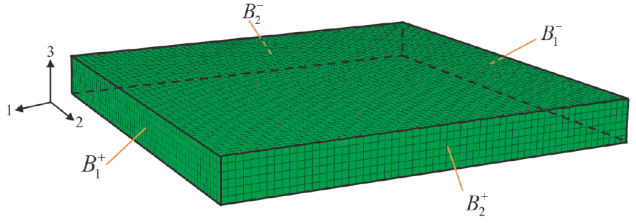

Figure 5 Schematic showing a discretized RVE subjected to PBCs.

Given that the RVE is under a macroscopic plane-stress condition for our calculations, the macroscopic Cauchy stress components Σ_{ii}, $i=1, 2$ are different from zero, which are computed by taking the volume average of the microscopic Cauchy stress components σ_{ii}

$$\Sigma_{ii}=\frac{1}{V}\int_V \sigma_{ii}\mathrm{d}V. \tag{24}$$

The macroscopic logarithmic strain components E_{ii}, $i=1, 2, 3$ are given by

$$E_{ii}=\ln(F_{ii}), \tag{25}$$

where F_{ii} are the diagonal components of the deformation

gradient **F**.

Thus, the von Mises equivalent stress and strain read

$$\begin{cases} \Sigma_{\rm eq} = \sqrt{\Sigma_{11}\Sigma_{11}+\Sigma_{22}\Sigma_{22}-\Sigma_{11}\Sigma_{22}}, \\ E_{\rm eq} = \dfrac{\sqrt{2}}{3}\sqrt{(E_{11}-E_{22})^2+(E_{11}-E_{33})^2+(E_{33}-E_{22})^2}. \end{cases} \tag{26}$$

3. Results and discussions

In this section, the influences of NS stress components (at the single crystal scale) on the stress/strain partitioning, stress-strain response, and yield surface (at the RVE scale) of DP steel are successively analyzed. For these purposes, at least one of the coefficients c_i (defined in Eq. (7)) is kept nonzero to account for the NS effects. As explained in Sect. 2.2.1, only c_1-c_4 are independent since the yield behavior is assumed to be independent of the hydrostatic stress in this study. Thus, we consider each coefficient c_i individually in order to isolate the effect of each NS stress component. The results are presented for a martensite volume fraction MVF = 19% for equiaxed and elongated microstructures. The insights derived from this section contribute to the understanding of the anisotropic-asymmetric plastic behavior exhibited by DP steels (as discussed in Refs. [28-31]).

To quantify the effect of c_i, a strength differential parameter SD measuring the T-C asymmetry is defined [61]

$$SD = \frac{2(\sigma_T-\sigma_C)}{\sigma_T+\sigma_C}, \tag{27}$$

where σ_T and σ_C denote the initial yield stress in tension and in compression, respectively. $SD = 0$ means no T-C asymmetry, which is the case when using the classical Schmid model. A positive SD corresponds to $\sigma_T > \sigma_C$, while a negative SD means $\sigma_T < \sigma_C$.

3.1 Stress/strain partitioning

In this subsection, the contours of the von Mises stress and maximum principal strain for equiaxed microstructure under uniaxial tension are plotted to visualize the stress and strain distributions. Figure 6 shows the stress and strain partitioning at $E_{\rm eq}$ = 0.03 with individual effect of each NS stress component. The case of $c_i = 0$ (without NS effects) is also presented as a reference, as shown in Fig. 6(a) and (b). It is noted that all the stress (resp. strain) contours share the same color bar with Fig. 6(a) (resp. Fig. 6(b)). It can be clearly seen from Fig. 6(a) that the harder martensite phases accommodate the majority of stress, as compared to the softer ferrite phases. On the other hand, the ferrite phases accommodate the majority of strain, as shown in Fig. 6(b). This is due to the fact that, in DP steels, the martensite phases contribute to the material strength, while the ferrite phases contribute to its ductility [4,62].

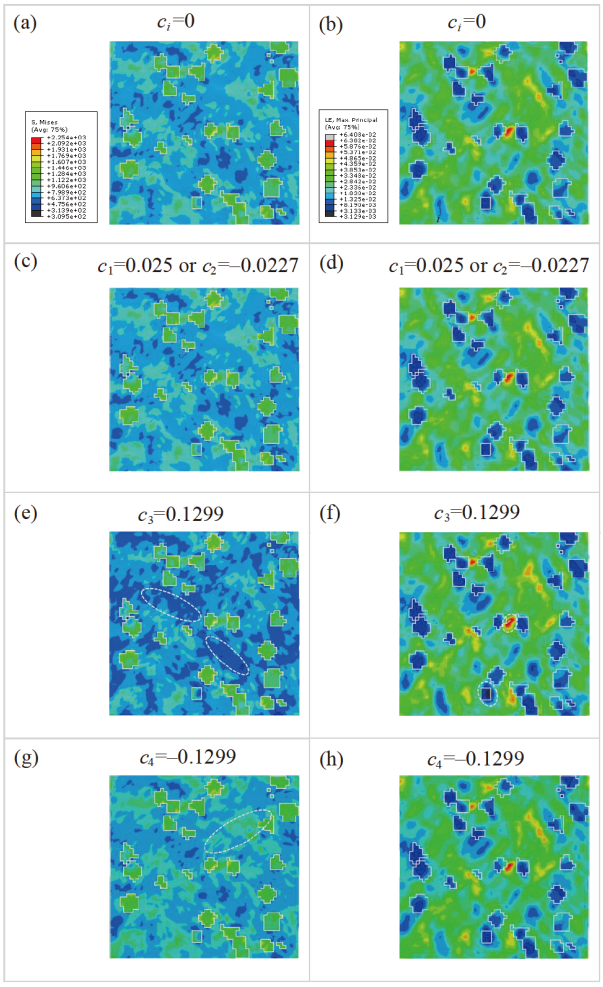

Figure 6 Effect of NS stress components on stress partitioning ((a), (c), (e), (g)) and strain partitioning ((b), (d), (f), (h)) of DP steel.

Then, the calculation is repeated by keeping $c_1 = 0.025$ and setting the other $c_i = 0$. As shown in Fig. 6(c) and (d), the prescribed value of c_1 does not lead to obvious change in the stress and strain distributions, as compared to the case without NS effects. The calculation is carried out for c_2 by keeping $c_2 = -0.0227$ and setting the other $c_i = 0$. Similar to the effect of c_1, the prescribed value of c_2 does not change the stress and strain distributions neither. The related contours are not presented for brevity (see also Fig. 6(c) and (d)). It is recalled that c_1 and c_2 are associated with the $\vec{\mathbf{t}} \otimes \vec{\mathbf{m}}$ and $\vec{\mathbf{t}} \otimes \vec{\mathbf{n}}$ NS shear stress components, respectively. Hence, the calculations suggest that these two shear stress components do not affect the local stress and strain concentrations in the studied DP steel.

In Fig. 6(e) and (f), the effect of the normal $\vec{\mathbf{n}} \otimes \vec{\mathbf{n}}$ NS stress component is revealed by prescribing only c_3 =0.1299. Figure 6(e) indicates that the increase in the value of the coefficient c_3 evidently decreases the local stress in the

ferrite phases (as marked by the open circles). On the other hand, Fig. 6(f) illustrates that the increase in parameter c_3 reduces the local strain in martensite phases, while enlarges that in ferrite phases (as marked by the open circles). These observations reveal that this NS stress component significantly affects both the stress and strain partitioning in the DP steel.

In Fig. 6(g) and (h), the effect of the normal $\vec{\mathbf{t}} \otimes \vec{\mathbf{t}}$ NS stress component is disclosed by keeping only $c_4 = -0.1299$. As can be seen in Fig. 6(g), the decrease in parameter c_4 intuitively changes the stress distribution in ferrite phases, as marked by the open circles. However, the change in component c_4 does not significantly influence the strain partitioning, as evidenced when comparing Fig. 6(b) to (h). These findings are further examined statistically.

For the purpose of clearer visualization, the distribution densities of stress and strain for the given values of c_i are presented at the same equivalent strain level, as shown in Fig. 7. The stress and strain values at the centroid of each element are included in the statistics. It can be seen from Fig. 7 that the distribution densities of stress and strain present two peaks, as respectively marked by the solid and dashed arrows. Evidently, the peak marked by the solid (resp. dashed) arrow is accommodated mainly by the ferrite (resp. martensite) phases. As a first observation, it is clear that the values assigned to coefficients c_1 and c_2 do not change the stress/strain partitioning in the studied DP steel, since the distribution density curves are coincident with those of $c_i = 0$. Importantly, the value assigned to parameter c_3 significantly decreases the local stress, as the corresponding curve (the blue one in Fig. 7(a)) moves left. However, the given value of component c_4 changes the stress partitioning very slightly. On the other hand, Fig. 7(b) illustrates that the given value of c_3 reduces the strain accommodation in the martensite phases and strengthens that in the ferrite phases, which validates the above contour analyses from a statistical viewpoint. Figure 7(b) also shows that the given value of c_4 mainly decreases the strain accommodation in ferrite phases, while does not affect the martensite phases. In a word, the increase in c_3 strongly intensifies both the stress and strain partitioning, whereas the decrease in c_4 slightly changes the stress accommodation in both phases, but apparently reduces the strain partitioning. Hence, the two normal NS stress components play important roles in the stress/strain partitioning of the studied DP steels.

3.2 Overall stress-strain response

In this subsection, we prescribe c_1-c_4, one at a time, in order to decouple the effects of NS stress components on the overall stress-strain response under tension and compression. In all of the figures presented in this subsection, "UT" or "UC" denotes uniaxial tension or uniaxial compression, while "0°" or "90°" designates the rolling direction or transverse direction, respectively. Both the equiaxed and elongated microstructures are considered in this analysis. Additionally, the overall stress-strain response without NS effects (i.e., $c_i = 0$) is also plotted as reference.

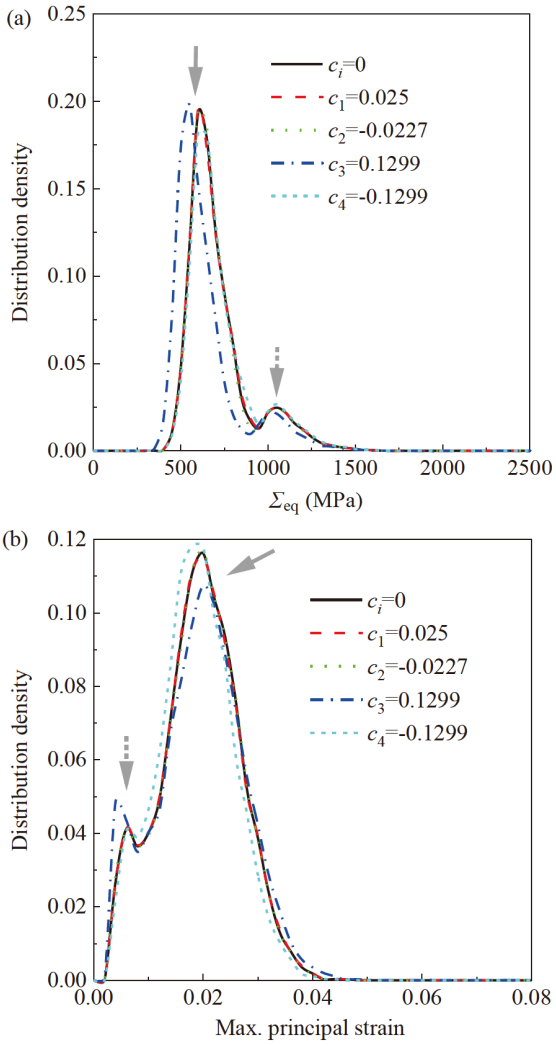

Figure 7 Distribution density of (a) equivalent stress and (b) maximum principal strain for the given individual NS coefficient c_i.

3.2.1 *Equiaxed microstructure*

The equiaxed microstructure, i.e., the microstructure with equiaxed phases and random grain orientations, is first considered. The equivalent stress-strain curves for $c_i \neq 0$ (NS effects with the full set of c_i values listed in Table 1), as well as for $c_i = 0$ (without NS effects), under UT and UC are plotted in Fig. 8(a). As can be seen in this figure, the four cases without NS effects show a coincident stress-strain response. This is well expected since the equiaxed microstructure with random grain orientations does not exhibit

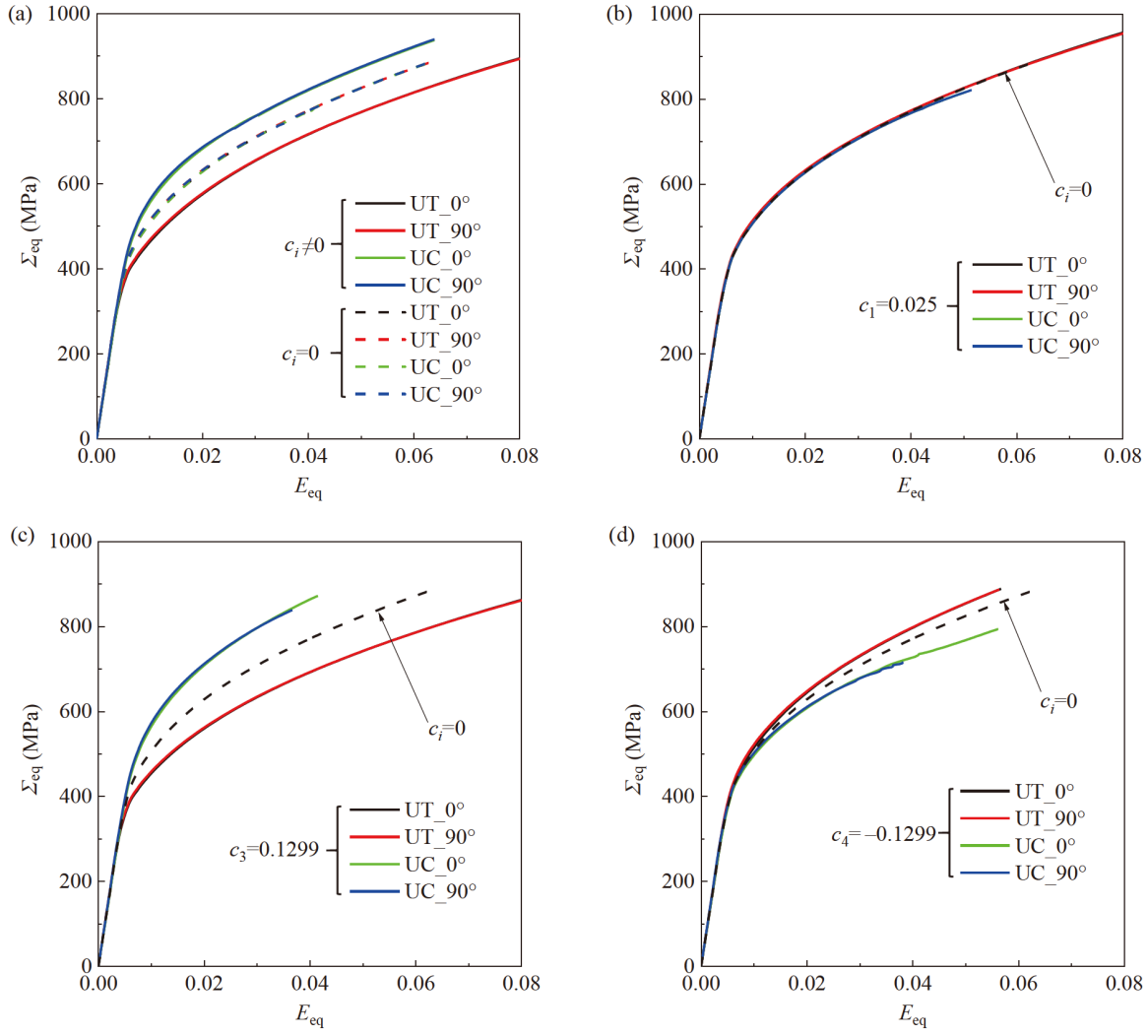

Figure 8 Effect of NS coefficients c_i on the stress-strain curve for the randomly oriented polycrystal with equiaxed microstructure. (a) $c_i \neq 0$; (b) $c_1 = 0.025$; (c) $c_3 = 0.1299$; (d) $c_4 = -0.1299$.

plastic anisotropy, and $c_i = 0$ (the classical Schmid law) does not involve T-C asymmetry. By contrast, the case of $c_i \neq 0$ (involving NS stress components) leads to obvious T-C asymmetry, manifesting that the flow stress in UC is larger than that in UT ($SD < 0$). Nevertheless, this set of c_i values does not induce obvious plastic anisotropy in DP steel.

Figure 8(b) shows the effect of c_1 ($\vec{\mathbf{t}} \otimes \vec{\mathbf{m}}$ NS shear stress component) on the stress-strain response by setting only $c_1 = 0.025$. As can be seen from this figure, $c_1 = 0.025$ leads to a negligible T-C asymmetry. The influence of a prescribed c_2 coefficient is similar to that of c_1, which is not presented here for brevity. Indeed, c_2 does not contribute to the T-C asymmetry, as demonstrated for BCC single crystals in the simulations conducted by Cho et al. [41] and the projection factor analysis reported by Lim et al. [42]. Additionally, a larger value for c_1 can result in apparent T-C asymmetry (see Fig. C1(a)). By contrast, a larger value for c_2 does not result in T-C asymmetry but leads to a change in the flow stress (see Fig. C1(b)).

The effect of c_3 is examined in Fig. 8(c). Unlike c_1 and c_2, $c_3 = 0.1299$ results in strong T-C asymmetry, where the flow stress in UC is significantly higher than that in UT (i.e., $SD < 0$). By contrast, the effect of c_4 is opposite to that of c_3 (as their signs are opposite), although c_4 leads to a weaker T-C asymmetry than c_3, as depicted in Fig. 8(d). The changes in c_i do not induce obvious plastic anisotropy for equiaxed microstructures, as illustrated in Fig. 8. It is worth noting that the simulation results reported by Cho et al. [41] reveal that the effects of c_i depend on the orientation of single crystals. Therefore, this motivates to conduct further studies on the effects of c_i in elongated polycrystals with crystallographic texture.

3.2.2 *Elongated microstructure*

The calculations performed in Sect. 3.2.1 are repeated here for elongated microstructures with crystallographic texture

(as defined in Sect. 2.1). In the same manner, the overall stress-strain curves for $c_i \neq 0$ (the same full set of c_i values used for the equiaxed microstructure), $c_1 = 0.025$, $c_2 = -0.0227$, $c_3 = 0.1299$, $c_4 = -0.1299$, under the loading scenarios UT_0°, UT_90°, UC_0°, and UC_90° are respectively plotted.

As shown in Fig. 9(a), when $c_i = 0$ (without NS effects), the stress-strain curves (the dashed curves) do not present T-C asymmetry but exhibit plastic anisotropy caused by the initial texture. When $c_i \neq 0$, the stress-strain curves (the solid curves) display both T-C asymmetry and plastic anisotropy. In Fig. 9(b), the effect of c_1 is examined by setting only $c_1 = 0.025$. It can be seen that the prescribed c_1 leads to slight T-C asymmetry. Actually, by comparing Fig. 8(b) with Fig. 9(b), on the one hand, and Fig. C1(a) with Fig. C2(a) (in Appendix C) on the other hand, it appears clear that the same change in c_1 for the textured microstructure leads to more pronounced T-C asymmetry than that for the equiaxed microstructure, suggesting that the texture effect exacerbates the NS effects. The effect of c_2 in the textured microstructure is similar to that in the equiaxed microstructure, which is not presented here for conciseness. It is important to emphasize that, although the prescribed values of c_1 and c_2 have minimal effects, they must be carefully evaluated, particularly for textured materials, as texture may intensify their impact.

The effects of c_3 and c_4 are studied in Fig. 9(c) and (d), respectively. These figures indicate that the effects of c_3 and c_4 on T-C asymmetry in textured microstructures are still similar, as compared to the cases of equiaxed microstructures. Figures 8 and 9, together with Figs. C1 and C2 (in Appendix C), suggest that the sign of *SD* hinges on the sign of c_i, and the impact of the sign of c_3 is the same as c_4, which is opposite to c_1. Moreover, the decoupled effect of c_i seems to not influence the plastic anisotropy in the textured

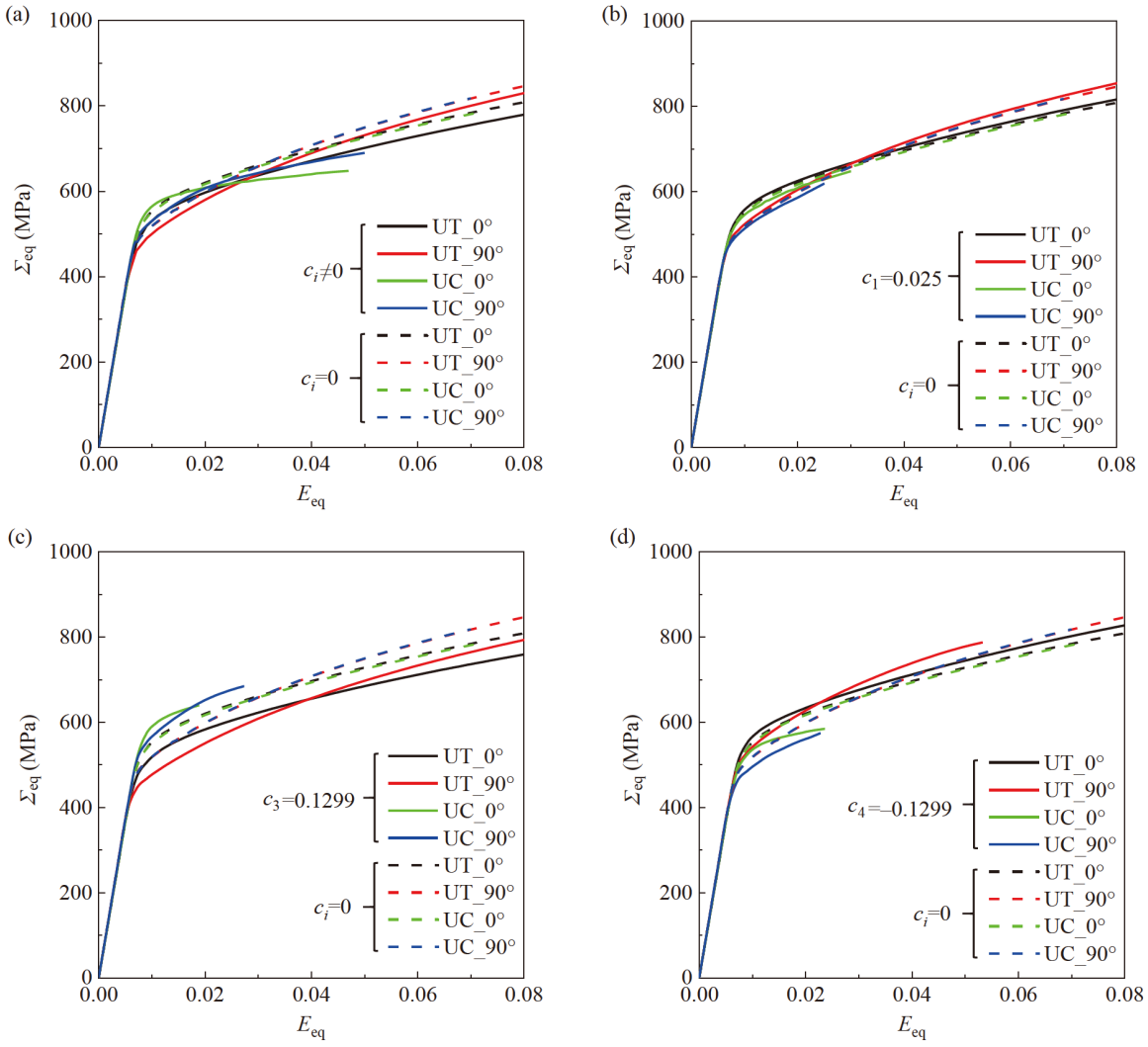

Figure 9 Effect of NS coefficients c_i on the stress-strain curve for the textured polycrystal with elongated microstructure. (a) $c_i \neq 0$; (b) $c_1 = 0.025$; (c) $c_3 = 0.1299$; (d) $c_4 = -0.1299$.

microstructure. However, the coupled effect of c_i indeed impacts the plastic anisotropy in the textured microstructure (see Fig. 9(a)), while not in the equiaxed one. This is likely due to the coupled texture and NS effects [33].

3.3 Yield surface

This subsection is devoted to revealing the effects of the NS stress components on the polycrystalline yield surface. Following the methodology in the previous subsection, the values for c_1-c_4 are individually prescribed to investigate their decoupled effects on the yield surface. To emphasize the shape change, the yield surfaces are normalized by the magnitude of yield stress in simple tension along the first principal axis.

3.3.1 Determination of yield surface

The polycrystalline yield surface for DP steel is presented in the Σ_{11}-Σ_{22} principal stress plane. In the calculation of the yield surface, Σ_{11} and Σ_{22} are kept proportional following the stress ratio:

$$\Sigma_{22}/\Sigma_{11} = \rho_{\Sigma}, \tag{28}$$

where $\rho_{\Sigma} = \tan\theta$ with $0° \le \theta < 360°$. A complete yield locus requires that θ varies from 0° to 360°. Equation (28) is enforced via the *MPC subroutine in ABAQUS [49]. Further technical details about the use of this constraint are provided in Ref. [59].

The Riemann Sum of the plastic work is defined following Ref. [33]:

$$W^p = \sum_{k=1}^{n} \left(E_{\mathrm{eq},k} - E_{\mathrm{eq},k-1}\right)\Sigma_{\mathrm{eq},k}, \tag{29}$$

where k stands for the strain increment numbering, while E_{eq} and Σ_{eq} are respectively the macroscopic equivalent strain and stress, as defined in Eq. (26).

The points on the yield surfaces are determined by a prescribed value of W^p, which ensures the equi-potential condition. The prescribed value of W^p is selected to be the value corresponding to a simple tension test at 0.2% plastic strain.

3.3.2 Equiaxed microstructure

The yield surfaces of equiaxed microstructure, with or without NS effects, are plotted in Fig. 10. The full set of c_i listed in Table 1 is first considered to obtain the yield surface with NS effects (denoted as $c_i \neq 0$). As can be seen from Fig. 10, the yield surface without NS effects ($c_i = 0$) approaches centrosymmetry, showing the absence of plastic anisotropy and T-C asymmetry ($SD = 0$). This is an expected outcome for the randomly oriented polycrystal with equiaxed microstructure. Figure 10 also shows that the NS effects ($c_i \neq 0$) clearly change the yield surface shape, thus reflecting the T-C asymmetry ($SD = -0.098$).

The case without NS effects ($c_i = 0$) is taken as reference to evaluate the effect of each NS stress component. To evaluate the effect of $\vec{\mathbf{t}} \otimes \vec{\mathbf{m}}$ NS shear stress, the computations are repeated by keeping the corresponding coefficient $c_1 = 0.025$, while setting the other $c_i = 0$. As shown in Fig. 11(a), the prescribed c_1 induces a negligible change in the shape of the yield surface. The prescribed c_2 ($\vec{\mathbf{t}} \otimes \vec{\mathbf{n}}$ NS shear stress) does not change the shape of the yield surface either, which is also shown in Fig. 11(a). Even varying their values, the NS stress components associated with c_1 and c_2 do not cause significant change in the yield surface of equiaxed microstructure, as revealed by Fig. C3 (see Appendix C).

In the same manner, the yield surfaces are plotted by prescribing only c_3 to study the effect of the normal $\vec{\mathbf{n}} \otimes \vec{\mathbf{n}}$ NS stress component. As shown in Fig. 11(b), the prescribed c_3 results in a pronounced expansion of the yield surface (except for the tension-tension (T-T) quadrant), which means that the yield becomes harder in compression

Σ_{22}

Figure 1
the rand

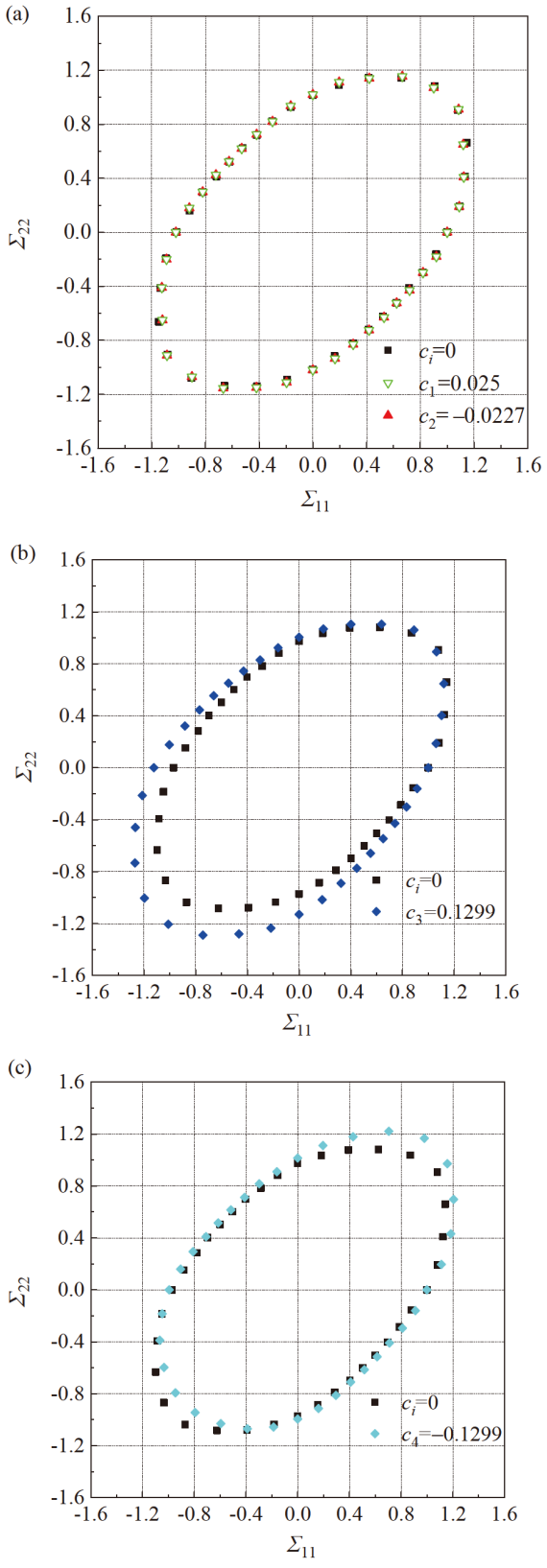

Figure 11 Effect of NS coefficients c_i on the yield surface projection in principal stress space for the randomly oriented polycrystal with equiaxed microstructure. (a) $c_1 = 0.025$ or $c_2 = -0.0227$; (b) $c_3 = 0.1299$; (c) $c_4 = -0.1299$.

harder yield in T-T stress state, while easier in C-C stress state. The opposite happens when c_4 is positive, i.e., harder yield in C-C stress state, while easier in T-T stress state.

On the whole, Figs. 10 and 11 depict that among the NS coefficients, c_3 and c_4 dictate the yield surface with NS effects. This means that, for equiaxed microstructures with random grain orientations, the NS normal stress components are of key importance in determining the yield surface, while the NS shear stress components can be neglected for that purpose. Whether this holds for textured microstructures will be addressed in the next subsection.

3.3.3 *Elongated microstructure*

The same series of computations are carried out for the textured microstructure with elongated phases. The case without NS effects is also included as reference, as marked by black solid squares in Fig. 12. As observed in Fig. 12, the yield surface without NS effects exhibits a vertex-type feature and slight plastic anisotropy due to the crystallographic texture. By contrast, the yield surface with NS effects reveals asymmetry in the equibiaxial states.

Figure 13(a) shows that the prescribed c_1 and c_2 do not induce obvious changes in yield surface. However, varying the values of c_1 or c_2 may result in significant changes in yield surface, as shown in Fig. C4 (Appendix C). This is different from the case of equiaxed microstructure (see Sect. 3.3.2), suggesting that there appear coupled texture and NS effects on the yield surface of textured microstructure.

Figure 13(b) depicts the effect of c_3 on the yield surface of textured microstructure. The prescribed c_3 leads to a stronger vertex-type feature in the T-T stress state, and harder yielding in the C-C stress state. Figure 13(c) shows the effect of c_4 on the yield surface of textured microstructure.

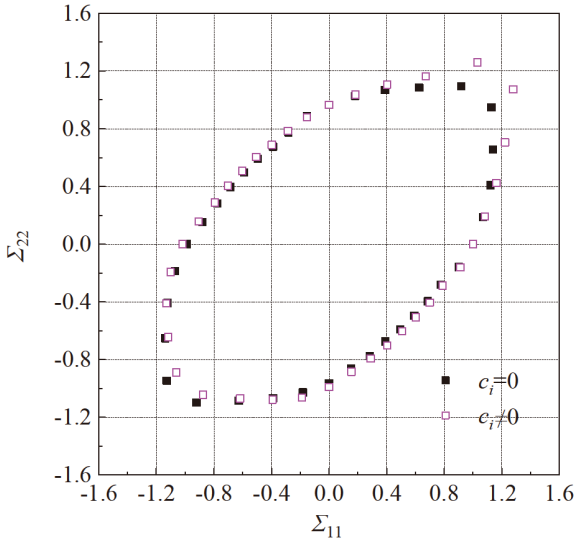

Figure 12 Yield surfaces with ($c_i \neq 0$) or without ($c_i = 0$) NS effects for the textured polycrystal with elongated microstructure.

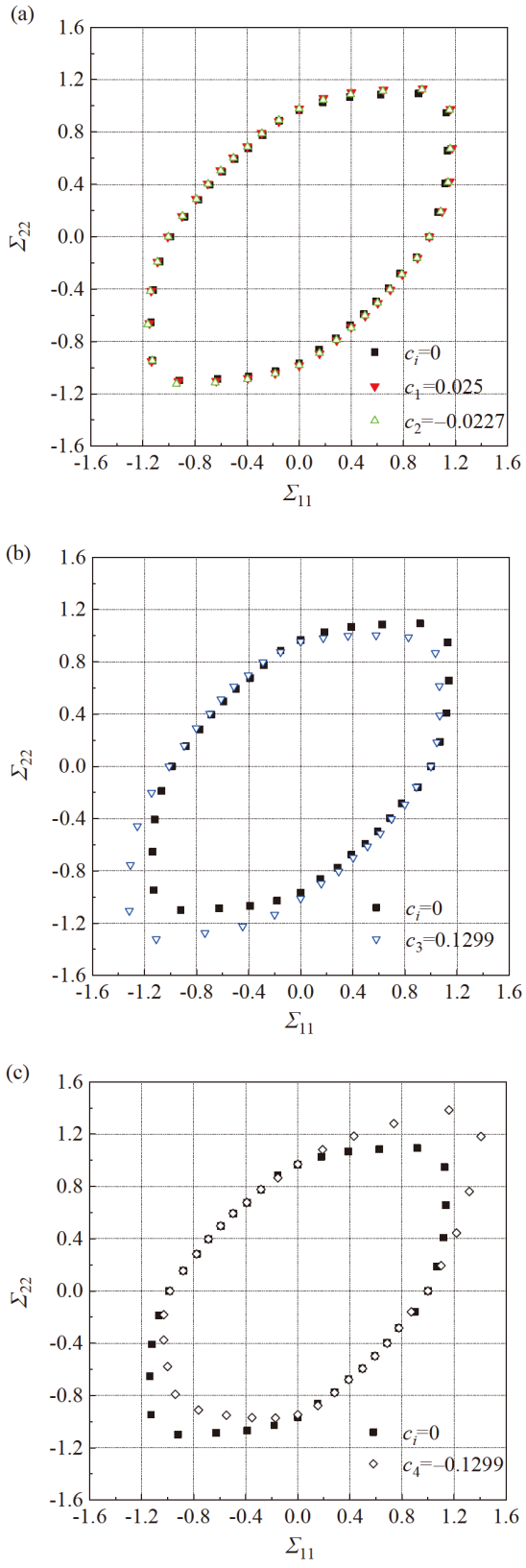

Figure 13 Effect of NS coefficients c_i on the yield surface projection in principal stress space for the textured polycrystal with elongated microstructure. (a) $c_1 = 0.025$ or $c_2 = -0.0227$; (b) $c_3 = 0.1299$; (c) $c_4 = -0.1299$.

Compared to Fig. 11(c), which shows the effect of c_4 for random microstructure, it is clear that the presence of texture amplifies the effect of c_4 on yield surface shape. Moreover, analyzing Figs. 12 and 13, it is concluded that the effect of c_4 dictates the yield surface of the studied textured microstructure, which is also different from the case of equiaxed microstructure.

The analyses in Sect. 3.3 reveals that the effects of c_i on the yield surfaces of random microstructure and of textured microstructure are different. This means that the effects of c_i depend on the crystallographic texture of the microstructure when determining the yield surfaces of DP steels.

3.4 Discussion

In the previous sections, the studied microstructure, characterized by grains elongated in the first direction due to the rolling process, exhibits anisotropy resulting from both crystallographic texture and grain morphology. When the NS effect is coupled with texture, the effect of grain morphology is inherently included. To specifically assess the impact of grain morphology, we create a new microstructure, i.e., randomly oriented polycrystal with elongated microstructure, denoted as "elongated-random". This new microstructure is compared with the original two from the previous sections: "equiaxed-random" (randomly oriented polycrystal with equiaxed microstructure) and "elongated-textured" (textured polycrystal with elongated microstructure). The "equiaxed-random" microstructure has shown the absence of plastic anisotropy (see Fig. 8(c)), indicating that random grain orientations do not induce plastic anisotropy. The tensile stress-strain curves along 0° and 90°, as well as the yield surfaces for these three microstructures, are presented when $c_3 = 0.1299$. As shown in Fig. 14(a), the "elongated-random" microstructure exhibits slight plastic anisotropy, attributed solely to grain morphology, since the grain orientations are random. Moreover, the stress-strain curves of this new microstructure are closer to those of the "equiaxed-random" microstructure. On the other hand, Fig. 14(b) reveals that the yield surface of the new microstructure closely resembles that of the "equiaxed-random" one. These trends demonstrate that, in the "elongated-textured" microstructure, although the combined texture and NS effects include the effect of grain morphology, the dominant factors are still the coupled crystallographic texture and NS effects.

In this paper, $MVF = 57\%$ (close to the MVF of DP980 steel) is chosen for calibrating the constitutive model parameters, while $MVF = 19\%$ (close to that of DP600 steel) is used for the formal discussion. The reason for this choice is twofold. Firstly, extensive experimental data, including both micropillar compression tests and macroscopic T-C strength

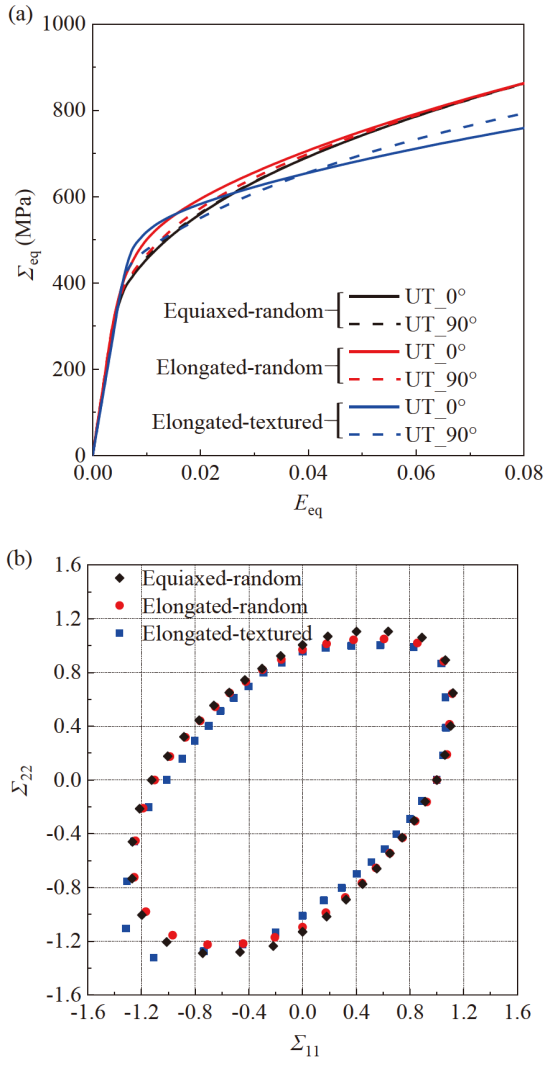

Figure 14 (a) Stress-strain curve and (b) yield surface for three microstructures when c_3=0.1299. "Equiaxed-random" (randomly oriented polycrystal with equiaxed microstructure), "elongated-random" (randomly oriented polycrystal with elongated microstructure), and "elongated-textured" (textured polycrystal with elongated microstructure).

differential tests for DP980 steel, are reported in Refs. [22,25,55]. The experimental data from these tests are sufficient for the appropriate identification of model parameters. Therefore, we did not conduct extra experimental tests for parameter identification, but directly used the existing data and set an MVF value of DP980. Secondly, the DP steel with *MVF* = 19% is chosen in Sect. 3 to highlight the NS effects in our study. Although the T-C strength differential effect cannot be neglected when accurately describing DP980, this effect in DP steels with a relatively low MVF is more evident, such as in DP600. This phenomenon is actually in line with the experimental data provided by Hou et al. [24], in which the plastic deformation of three DP steels (DP590, DP780, and DP980, DP980 having the highest MVF, followed by DP780 and then DP590) is characterized under several loading paths (see Figs. 6 and 8 therein). In fact, the effect of c_i is shown to be weaker when the MVF increases from 0.19 to 0.57, the pertaining results are not duplicated here to keep the paper at a reasonable length.

4. Conclusion

In this work, a dislocation density-based crystal plasticity model is used to study the NS effects in ferrite-martensite DP steels. In the model, the NS stress terms are incorporated only for the ferrite phases, which are shown to exhibit NS effects. The influences of NS stress components on the mechanical response of DP steels are analyzed, including stress/strain partitioning, plastic flow, and yield surface. Two kinds of microstructures commonly observed in DP steels are considered: equiaxed phases with random grain orientations, and elongated phases with crystallographic texture. The main conclusions are summarized as follows:

(1) The NS stress components, especially the normal components, significantly impact the stress and strain partitioning.

(2) The normal $\vec{\mathbf{n}}\otimes\vec{\mathbf{n}}$ component is also the main contributor to T-C asymmetry for random equiaxed microstructures. For the textured elongated microstructures, a combined influence of crystallographic texture and NS effect is observed.

(3) The effects of NS stress components depend on the crystallographic texture of the microstructure when determining the yield surface.

These findings shed light on the nuanced interplay between NS effects, microstructural characteristics, and mechanical behavior in DP steels, providing valuable insights into the role of crystallographic texture and NS stress components in governing the material response under various loading conditions.

Appendix A. Slip systems

For the ferrite phase (Table A1), we focus on the $\{110\}\langle111\rangle$ slip systems with NS effects, since the geometry of $1/2\langle111\rangle$ screw dislocations on the $\{110\}$ planes has been better understood in experiments and atomistic simulations [22,41]. Importantly, it should be noted that the slip systems α = 13-24 are conjugated to α = 1-12, with the only difference being the sign of slip direction $\vec{\mathbf{m}}^{\alpha}$. Within the classical Schmid law, the conjugate pairs of slip systems are degenerated to the 12 original ones. However, within the NS crystal plasticity, the full set of 24-$\{110\}\langle111\rangle$ slip systems should be used because the NS stresses are different between slip systems α = 1-12 and α = 13-24 [41]. For the martensite phase (Table A2), the 12-$\{110\}\langle111\rangle$ and 12-$\{112\}\langle111\rangle$ slip systems are used.

Table A1 Slip systems for ferrite phase

	$\vec{\mathbf{m}}^{\alpha}$	$\vec{\mathbf{n}}^{\alpha}$		$\vec{\mathbf{m}}^{\alpha}$	$\vec{\mathbf{n}}^{\alpha}$
1	[111]	$(01\bar{1})$	13	$[\bar{1}\bar{1}\bar{1}]$	$(01\bar{1})$
2	[111]	$(\bar{1}01)$	14	$[\bar{1}\bar{1}\bar{1}]$	$(\bar{1}01)$
3	[111]	$(1\bar{1}0)$	15	$[\bar{1}\bar{1}\bar{1}]$	$(1\bar{1}0)$
4	$[\bar{1}11]$	$(\bar{1}0\bar{1})$	16	$[1\bar{1}\bar{1}]$	$(\bar{1}0\bar{1})$
5	$[\bar{1}11]$	$(0\bar{1}1)$	17	$[1\bar{1}\bar{1}]$	$(0\bar{1}1)$
6	$[\bar{1}11]$	(110)	18	$[1\bar{1}\bar{1}]$	(110)
7	$[\bar{1}\bar{1}1]$	$(0\bar{1}\bar{1})$	19	$[11\bar{1}]$	$(0\bar{1}\bar{1})$
8	$[\bar{1}\bar{1}1]$	(101)	20	$[11\bar{1}]$	(101)
9	$[\bar{1}\bar{1}1]$	$(\bar{1}10)$	21	$[11\bar{1}]$	$(\bar{1}10)$
10	$[1\bar{1}1]$	$(10\bar{1})$	22	$[\bar{1}1\bar{1}]$	$(10\bar{1})$
11	$[1\bar{1}1]$	(011)	23	$[\bar{1}1\bar{1}]$	(011)
12	$[1\bar{1}1]$	$(\bar{1}\bar{1}0)$	24	$[\bar{1}1\bar{1}]$	$(\bar{1}\bar{1}0)$

Table A2 Slip systems for martensite phase

	$\vec{\mathbf{m}}^{\alpha}$	$\vec{\mathbf{n}}^{\alpha}$		$\vec{\mathbf{m}}^{\alpha}$	$\vec{\mathbf{n}}^{\alpha}$
1	[111]	$(01\bar{1})$	13	[111]	$(11\bar{2})$
2	[111]	$(\bar{1}01)$	14	[111]	$(1\bar{2}1)$
3	[111]	$(1\bar{1}0)$	15	[111]	$(\bar{2}11)$
4	$[\bar{1}11]$	$(\bar{1}0\bar{1})$	16	$[\bar{1}11]$	$(1\bar{1}2)$
5	$[\bar{1}11]$	$(0\bar{1}1)$	17	$[\bar{1}11]$	$(12\bar{1})$
6	$[\bar{1}11]$	(110)	18	$[\bar{1}11]$	(211)
7	$[\bar{1}\bar{1}1]$	$(0\bar{1}\bar{1})$	19	$[\bar{1}\bar{1}1]$	(112)
8	$[\bar{1}\bar{1}1]$	(101)	20	$[\bar{1}\bar{1}1]$	$(\bar{1}21)$
9	$[\bar{1}\bar{1}1]$	$(\bar{1}10)$	21	$[\bar{1}\bar{1}1]$	$(2\bar{1}1)$
10	$[1\bar{1}1]$	$(10\bar{1})$	22	$[1\bar{1}1]$	$(\bar{1}12)$
11	$[1\bar{1}1]$	(011)	23	$[1\bar{1}1]$	(121)
12	$[1\bar{1}1]$	$(\bar{1}\bar{1}0)$	24	$[1\bar{1}1]$	$(21\bar{1})$

Appendix B. Finite element model setting for the micropillar compression simulations

A finite element model is used to mimic the micropillar compression experiments of Chen et al. [22]. The diameter of the micropillar is set to 2 μm and the height-to-diameter ratio is taken to be 2. These geometric characteristics are in line with the dimensions of the experimental specimens. The top face of the micropillar model is indented by a flat rigid surface representing the flat punch. The friction coefficient is set to 0.5 in the simulations, to account for the interaction between the punch and micropillars, in the same way as in Ref. [22]. The micropillars are discretized using 2400 eight-node hexahedral finite elements. The micropillar compression simulations are conducted for [205], [326], [324]-oriented ferrite micropillars, and a martensite micropillar with multiple blocks. The relevant von Mises stress contours obtained by finite element computations are provided in Fig. B1.

Appendix C. Stress-strain curves and yield surfaces by varying NS coefficients c_1 and c_2

For the random polycrystal with equiaxed microstructure, the stress-strain curves are plotted by setting $c_1 = 0.5$[1)] and $c_2 = 0.5$, successively, as shown in Fig. C1(a) and (b), respectively. Figure C1(a) reveals that $c_1 = 0.5$ results in an obvious T-C asymmetry. Figure C1(b) depicts that $c_2 = 0.5$ does not lead to T-C asymmetry but induces a noticeable change in the flow stress level.

For the textured polycrystal with elongated microstructure, the stress-strain curves are plotted by setting $c_1 = 0.5$ and $c_2 = 0.5$, successively, as shown in Fig. C2(a)

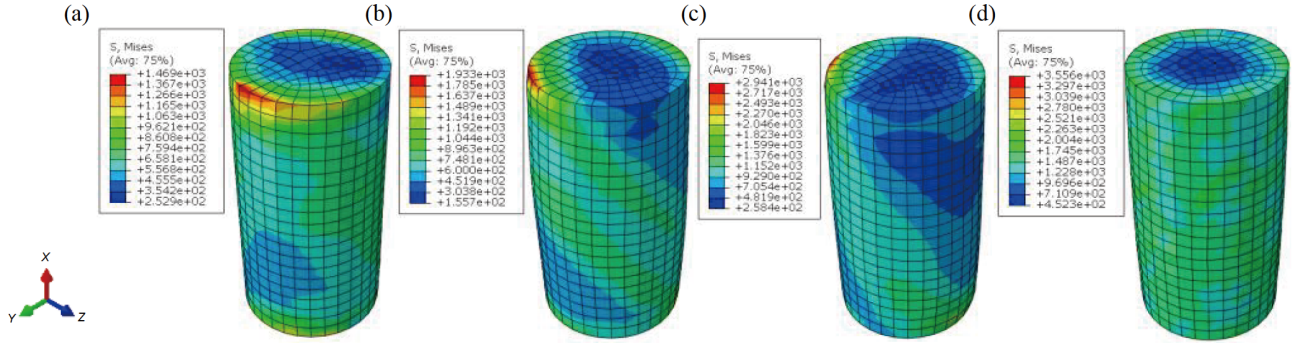

Figure B1 Von Mises stress contours of ferrite and martensite micropillars at 5% strain: (a) [205]-oriented ferrite micropillar; (b) [326]-oriented ferrite micropillar; (c) [324]-oriented ferrite micropillar; (d) martensite micropillar with multiple blocks.

1) In this appendix, the NS coefficients c_1 and c_2 are taken to be 0.5 (or −0.5) to amplify their effects. Such relatively large values of NS coefficients have been used to characterize the mechanical response of tantalum at low temperature [63]. Here, it is noted that the use of large coefficients does not mean they can be achieved for DP steels at low temperature because of the lack of relevant experimental reports.

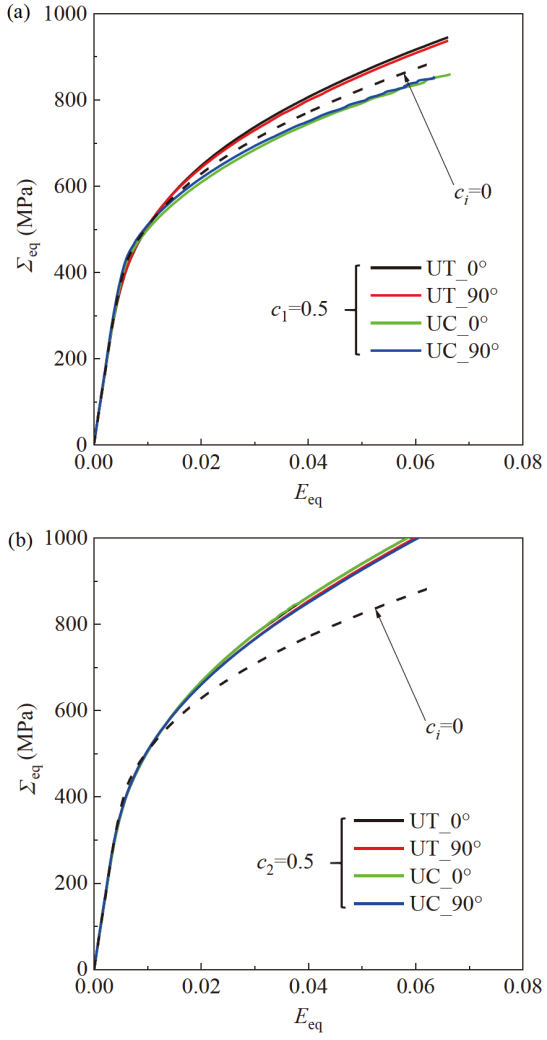

Figure C1 Stress-strain curves with (a) $c_1 = 0.5$ and (b) $c_2 = 0.5$ for the random polycrystal with equiaxed microstructure.

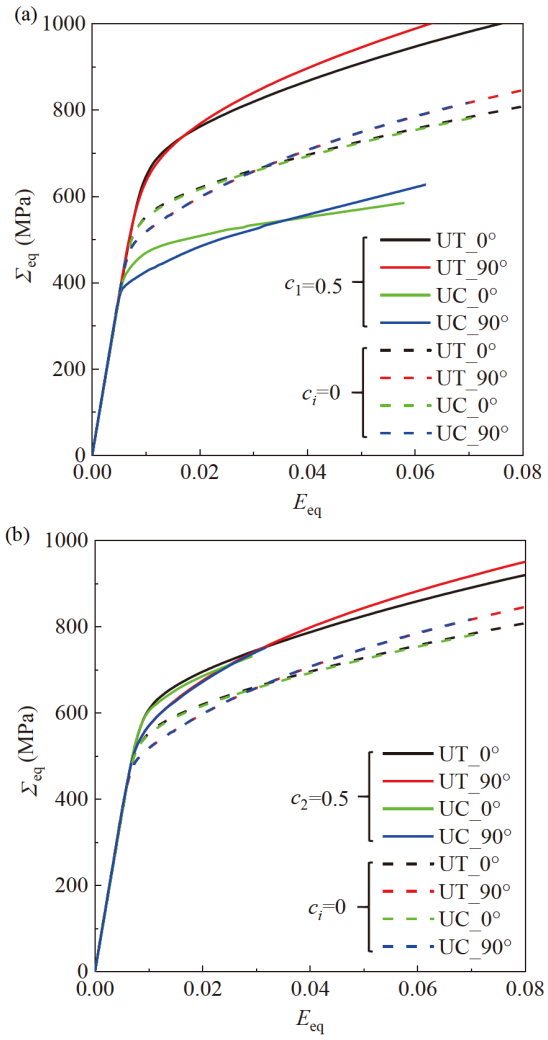

Figure C2 Stress-strain curves with (a) $c_1 = 0.5$ and (b) $c_2 = 0.5$ for the textured polycrystal with elongated microstructure.

and (b), respectively. Figure C2(a) reveals that $c_1 = 0.5$ results in stronger T-C asymmetry in textured microstructure, as compared to the case of equiaxed microstructure (see Figs. C1(a)) and C2(b) shows that $c_2 = 0.5$ does not induce T-C asymmetry, but induces a change in the flow stress level, which is similar to the case of equiaxed microstructure.

For the random polycrystal with equiaxed microstructure, the yield surfaces are plotted by varying c_1 and c_2, successively, as shown in Fig. C3(a) and (b), respectively. Figure C3(a) suggests that the variation of c_1 leads to a subtle change in the yield surface of equiaxed microstructure. Also, the variation of c_2 results in a negligible change in the yield surface, as revealed in Fig. C3(b).

For the textured polycrystal with elongated microstructure, the yield surfaces are plotted by varying c_1 and c_2, successively, as shown in Fig. C4(a) and (b), respectively. It can be seen from Fig. C4(a) that, as c_1 decreases from 0 to -0.5, the locus in the T-T stress state exhibits a stronger vertex-type feature, whereas the yield in the C-C stress state becomes much harder. The opposite happens when c_1 increases from 0 to 0.5, where the yield in the T-T stress state becomes harder. It is evident from Fig. C4(b) that the yield surface becomes shortened and obtuse along $\Sigma_{11} - \Sigma_{22} = 0$ as c_2 increases from -0.5 to 0.5. This means that the yield in T-T and C-C stress states becomes easier as c_2 increases.

Conflict of interest *On behalf of all authors, the corresponding author states that there is no conflict of interest.*

Author contributions *Jianchang Zhu designed the research and wrote the first draft of the manuscript. Mohamed Ben Bettaieb helped develop software code. Zhenhuan Li and Minsheng Huang helped organize the manuscript. Farid Abed-Meraim revised and edited the final version.*

Acknowledgements *This work was supported by the National Natural Science Foundation of China (Grant Nos. 12202153 and 12072123).*

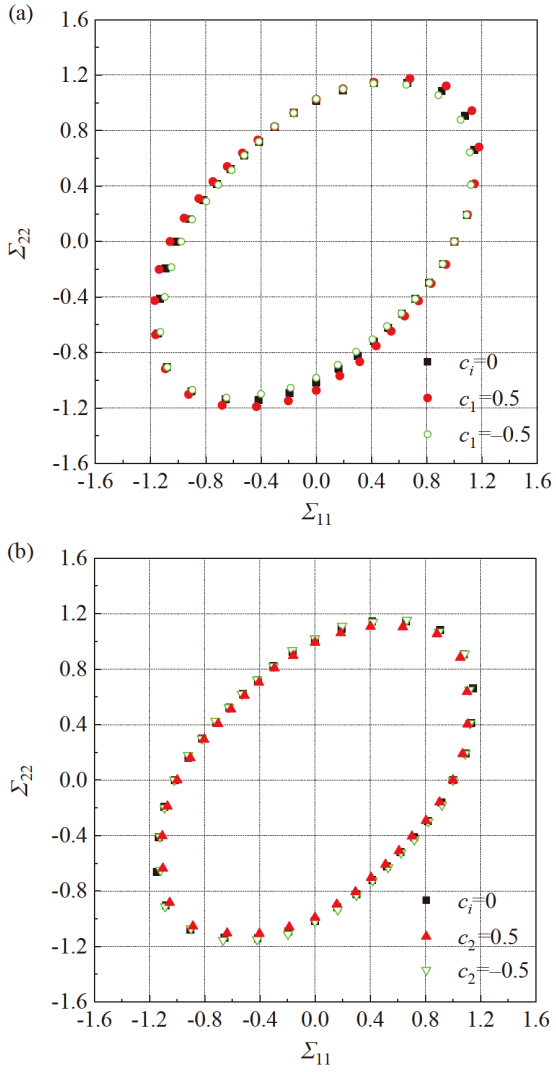

Figure C3 Yield surface projections in principal stress space for the random polycrystal with equiaxed microstructure, by varying NS coefficients c_1 and c_2. (a) $c_1 = 0.5$ or $c_1 = -0.5$; (b) $c_2 = 0.5$ or $c_2 = -0.5$.

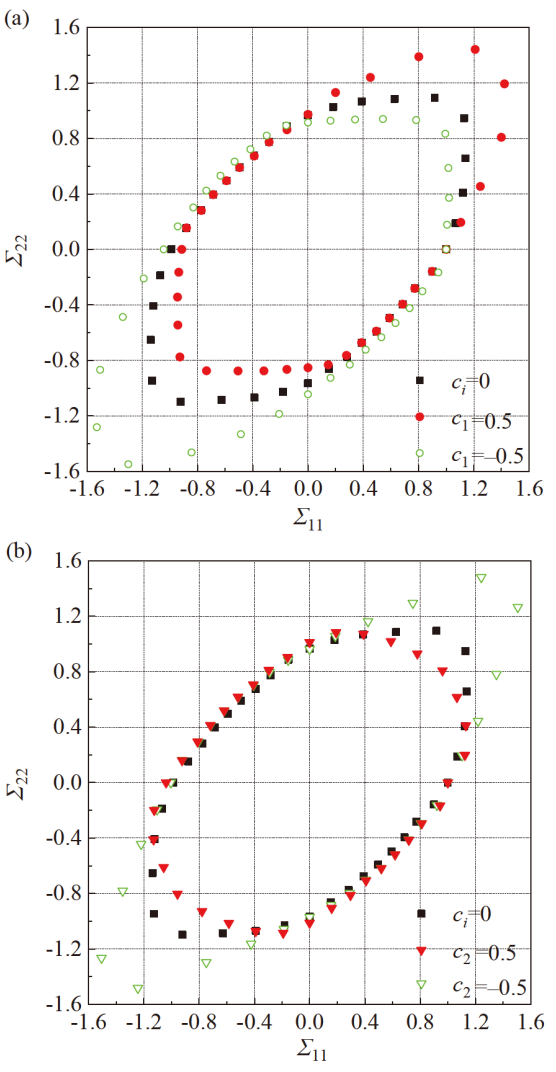

Figure C4 Yield surface projections in principal stress space for the textured polycrystal with elongated microstructure, by varying NS coefficients c_1 and c_2. (a) $c_1 = 0.5$ or $c_1 = -0.5$; (b) $c_2 = 0.5$ or $c_2 = -0.5$.

1 N. H. Abid, R. K. Abu Al-Rub, and A. N. Palazotto, Micromechanical finite element analysis of the effects of martensite morphology on the overall mechanical behavior of dual phase steel, Int. J. Solids Struct. **104-105**, 8 (2017).

2 Q. Lai, L. Brassart, O. Bouaziz, M. Gouné, M. Verdier, G. Parry, A. Perlade, Y. Bréchet, and T. Pardoen, Influence of martensite volume fraction and hardness on the plastic behavior of dual-phase steels: Experiments and micromechanical modeling, Int. J. Plast. **80**, 187 (2016).

3 A. P. Pierman, O. Bouaziz, T. Pardoen, P. J. Jacques, and L. Brassart, The influence of microstructure and composition on the plastic behaviour of dual-phase steels, Acta Mater. **73**, 298 (2014).

4 S. Basu, A. Patra, B. N. Jaya, S. Ganguly, M. Dutta, and I. Samajdar, Study of microstructure-property correlations in dual phase steels for achieving enhanced strength and reduced strain partitioning, Materialia **25**, 101522 (2022).

5 F. Briffod, T. Shiraiwa, and M. Enoki, Micromechanical investigation of the effect of the crystal orientation on the local deformation path and ductile void nucleation in dual-phase steels, Mater. Sci. Eng.-A **826**, 141933 (2021).

6 S. O. Çakmak, and T. Yalçinkaya, Morphology and grain orientation dependent localization and necking in dual-phase steels, Procedia Struct. Integr. **21**, 224 (2019).

7 M. Jafari, N. Saeidi, S. Ziaei-Rad, M. Jamshidian, and H. S. Kim, Micromechanical analysis of orientation dependency on deformation behavior in DP steels by dislocation density-based crystal plasticity simulation, Mech. Mater. **134**, 132 (2019).

8 Y. Hou, S. Cai, T. Sapanathan, A. Dumon, and M. Rachik, Micromechanical modeling of the effect of phase distribution topology on the plastic behavior of dual-phase steels, Comput. Mater. Sci. **158**, 243 (2019).

9 M. Marvi-Mashhadi, M. Mazinani, and A. Rezaee-Bazzaz, FEM modeling of the flow curves and failure modes of dual phase steels with different martensite volume fractions using actual microstructure as the representative volume, Comput. Mater. Sci. **65**, 197 (2012).

10 S. K. Paul, Effect of martensite volume fraction on stress triaxiality and deformation behavior of dual phase steel, Mater. Des. **50**, 782 (2013).

11 X. Sun, K. S. Choi, W. N. Liu, and M. A. Khaleel, Predicting failure modes and ductility of dual phase steels using plastic strain localization, Int. J. Plast. **25**, 1888 (2009).

12 T. Matsuno, C. Teodosiu, D. Maeda, and A. Uenishi, Mesoscale

simulation of the early evolution of ductile fracture in dual-phase steels, Int. J. Plast. **74**, 17 (2015).
13 F. Barlat, G. Vincze, J. J. Grácio, M. G. Lee, E. F. Rauch, and C. N. Tomé, Enhancements of homogenous anisotropic hardening model and application to mild and dual-phase steels, Int. J. Plast. **58**, 201 (2014).
14 J. Liao, J. A. Sousa, A. B. Lopes, X. Xue, F. Barlat, and A. B. Pereira, Mechanical, microstructural behaviour and modelling of dual phase steels under complex deformation paths, Int. J. Plast. **93**, 269 (2017).
15 S. Y. P. Allain, O. Bouaziz, I. Pushkareva, and C. P. Scott, Towards the microstructure design of DP steels: A generic size-sensitive mean-field mechanical model, Mater. Sci. Eng.-A **637**, 222 (2015).
16 E. Espinosa, A. Sardar, C. H. M. Simha, and A. Bardelcik, Realistic morphology-based Representative Volume Elements for dual-phase steels, Mech. Mater. **160**, 103961 (2021).
17 T. Yalçinkaya, S. O. Çakmak, and C. Tekoğlu, A crystal plasticity based finite element framework for RVE calculations of two-phase materials: Void nucleation in dual-phase steels, Finite Elem. Anal. Des. **187**, 103510 (2021).
18 J. Kadkhodapour, A. Butz, S. Ziaei-Rad, and S. Schmauder, A micro mechanical study on failure initiation of dual phase steels under tension using single crystal plasticity model, Int. J. Plast. **27**, 1103 (2011).
19 M. Jafari, S. Ziaei-Rad, N. Saeidi, and M. Jamshidian, Micromechanical analysis of martensite distribution on strain localization in dual phase steels by scanning electron microscopy and crystal plasticity simulation, Mater. Sci. Eng.-A **670**, 57 (2016).
20 T. Vermeij, C. J. A. Mornout, V. Rezazadeh, and J. P. M. Hoefnagels, Martensite plasticity and damage competition in dual-phase steel: A micromechanical experimental-numerical study, Acta Mater. **254**, 119020 (2023).
21 C. C. Tasan, J. P. M. Hoefnagels, M. Diehl, D. Yan, F. Roters, and D. Raabe, Strain localization and damage in dual phase steels investigated by coupled in-situ deformation experiments and crystal plasticity simulations, Int. J. Plast. **63**, 198 (2014).
22 P. Chen, H. Ghassemi-Armaki, S. Kumar, A. Bower, S. Bhat, and S. Sadagopan, Microscale-calibrated modeling of the deformation response of dual-phase steels, Acta Mater. **65**, 133 (2014).
23 A. Srivastava, A. F. Bower, L. G. Hector, J. E. Carsley, L. Zhang, and F. Abu-Farha, A multiscale approach to modeling formability of dual-phase steels, Model. Simul. Mater. Sci. Eng. **24**, 025011 (2016).
24 Y. Hou, J. Min, N. Guo, J. Lin, J. E. Carsley, T. B. Stoughton, H. Traphöner, T. Clausmeyer, and A. E. Tekkaya, Investigation of evolving yield surfaces of dual-phase steels, J. Mater. Process. Tech. **287**, 116314 (2021).
25 T. Maeda, N. Noma, T. Kuwabara, F. Barlat, and Y. P. Korkolis, Experimental verification of the tension-compression asymmetry of the flow stresses of a high strength steel sheet, Procedia Eng. **207**, 1976 (2017).
26 H. Mehrabi, R. C. Yang, and B. Wang, Effects of tension-compression asymmetry on bending of steels, Appl. Sci. **10**, 3339 (2020).
27 N. Noma, and T. Kuwabara, Material modeling and springback analysis considering tension/compression asymmetry of flow stresses, Key Eng. Mater. **611-612**, 33 (2014).
28 Y. Lou, and J. W. Yoon, Lode-dependent anisotropic-asymmetric yield function for isotropic and anisotropic hardening of pressure-insensitive materials. Part I: Quadratic function under non-associated flow rule, Int. J. Plast. **166**, 103647 (2023).
29 Y. Hou, J. Min, T. B. Stoughton, J. Lin, J. E. Carsley, and B. E. Carlson, A non-quadratic pressure-sensitive constitutive model under non-associated flow rule with anisotropic hardening: Modeling and validation, Int. J. Plast. **135**, 102808 (2020).
30 Y. Hou, J. Min, A. A. El-Aty, H. N. Han, and M. G. Lee, A new anisotropic-asymmetric yield criterion covering wider stress states in sheet metal forming, Int. J. Plast. **166**, 103653 (2023).
31 S. Y. Lee, J. H. Kim, and F. Barlat, Appropriateness of hydrostatic pressure-based modeling for strength differential effect in advanced high strength steel, Mech. Mater. **186**, 104807 (2023).
32 X. Yang, J. Zhao, B. Du, Y. Guo, and Y. Li, The yielding and plastic flow behavior of TC17 alloy under tension/compression-torsion loading at high strain rates, Acta Mech. Sin. **40**, 423420 (2024).
33 D. J. Savage, I. J. Beyerlein, and M. Knezevic, Coupled texture and non-Schmid effects on yield surfaces of body-centered cubic polycrystals predicted by a crystal plasticity finite element approach, Int. J. Solids Struct. **109**, 22 (2017).
34 M. A. Groeber, and M. A. Jackson, DREAM.3D: A digital representation environment for the analysis of microstructure in 3D, Integr. Mater. Manuf. Innov. **3**, 56 (2014).
35 A. Ramazani, Z. Ebrahimi, and U. Prahl, Study the effect of martensite banding on the failure initiation in dual-phase steel, Comput. Mater. Sci. **87**, 241 (2014).
36 G. Bian, F. Liu, T. Zhang, M. Ran, X. Xue, D. Wu, and W. Wang, Elongation enhancement strategies for AISI 430 stainless steel welded joints : Insights from molecular dynamics analysis, Acta Mech. Sin. **41**, 424019 (2025).
37 A. Ch. Darabi, H. R. Chamani, J. Kadkhodapour, A. P. Anaraki, A. Alaie, and M. R. Ayatollahi, Micromechanical analysis of two heat-treated dual phase steels: DP800 and DP980, Mech. Mater. **110**, 68 (2017).
38 M. R. Ayatollahi, A. C. Darabi, H. R. Chamani, and J. Kadkhodapour, 3D micromechanical modeling of failure and damage evolution in dual phase steel based on a real 2D microstructure, Acta Mech. Solid Sin. **29**, 95 (2016).
39 A. Cheloee Darabi, J. Kadkhodapour, A. Pourkamali Anaraki, M. Khoshbin, A. Alaie, and S. Schmauder, Micromechanical modeling of damage mechanisms in dual-phase steel under different stress states, Eng. Fract. Mech. **243**, 107520 (2021).
40 C. R. Weinberger, C. C. Battaile, T. E. Buchheit, and E. A. Holm, Incorporating atomistic data of lattice friction into BCC crystal plasticity models, Int. J. Plast. **37**, 16 (2012).
41 H. Cho, C. A. Bronkhorst, H. M. Mourad, J. R. Mayeur, and D. J. Luscher, Anomalous plasticity of body-centered-cubic crystals with non-Schmid effect, Int. J. Solids Struct. **139-140**, 138 (2018).
42 H. Lim, C. R. Weinberger, C. C. Battaile, and T. E. Buchheit, Application of generalized non-Schmid yield law to low-temperature plasticity in bcc transition metals, Model. Simul. Mater. Sci. Eng. **21**, 045015 (2013).
43 H. Lim, L. M. Hale, J. A. Zimmerman, C. C. Battaile, and C. R. Weinberger, A multi-scale model of dislocation plasticity in α-Fe: Incorporating temperature, strain rate and non-Schmid effects, Int. J. Plast. **73**, 100 (2015).
44 M. Knezevic, I. J. Beyerlein, M. L. Lovato, C. N. Tomé, A. W. Richards, and R. J. McCabe, A strain-rate and temperature dependent constitutive model for BCC metals incorporating non-Schmid effects: Application to tantalum-tungsten alloys, Int. J. Plast. **62**, 93 (2014).
45 R. Gröger, V. Racherla, J. L. Bassani, and V. Vitek, Multiscale modeling of plastic deformation of molybdenum and tungsten: II. Yield criterion for single crystals based on atomistic studies of glide of $1/2\langle 111\rangle$ screw dislocations, Acta Mater. **56**, 5412 (2008).
46 M. G. Lee, H. Lim, B. L. Adams, J. P. Hirth, and R. H. Wagoner, A dislocation density-based single crystal constitutive equation, Int. J. Plast. **26**, 925 (2010).
47 M. Ben Bettaieb, O. Débordes, A. Dogui, L. Duchêne, and C. Keller, On the numerical integration of rate independent single crystal behavior at large strain, Int. J. Plast. **32-33**, 184 (2012).
48 U. F. Kocks, Laws for work-hardening and low-temperature creep, J. Eng. Mater. Tech. **98**, 76 (1976).
49 Abaqus. ABAQUS Version 6.14. Dassault Systèmes Simulia Corp, Provid RI 2014.
50 H. K. Akpama, M. B. Bettaieb, and F. Abed-Meraim, Numerical integration of rate-independent BCC single crystal plasticity models: Comparative study of two classes of numerical algorithms, Numer. Meth. Eng. **108**, 363 (2016).
51 H. K. Akpama, M. Ben Bettaieb, and F. Abed-Meraim, Localized

necking predictions based on rate-independent self-consistent polycrystal plasticity: Bifurcation analysis versus imperfection approach, Int. J. Plast. **91**, 205 (2017).
52 L. Yu, W. Liu, H. Sui, Y. Liu, and H. Duan, A dislocation-based model for cyclic plastic response of lath martensitic steels, Acta Mech. Sin. **38**, 421353 (2022).
53 A. Mapar, H. Ghassemi-Armaki, F. Pourboghrat, and K. S. Kumar, A differential-exponential hardening law for non-Schmid crystal plasticity finite element modeling of ferrite single crystals, Int. J. Plast. **91**, 268 (2017).
54 A. Patra, T. Zhu, and D. L. McDowell, Constitutive equations for modeling non-Schmid effects in single crystal bcc-Fe at low and ambient temperatures, Int. J. Plast. **59**, 1 (2014).
55 T. Maeda, N. Noma, T. Kuwabara, F. Barlat, and Y. P. Korkolis, Measurement of the strength differential effect of DP980 steel sheet and experimental validation using pure bending test, J. Mater. Process. Tech. **256**, 247 (2018).
56 K. Yoshida, An alternative formulation of two-grain cluster model for homogenization of elastoviscoplastic behavior of polycrystal, Int. J. Plast. **156**, 103368 (2022).
57 A. Eghtesad, and M. Knezevic, High-performance full-field crystal plasticity with dislocation-based hardening and slip system back-stress laws: Application to modeling deformation of dual-phase steels, J. Mech. Phys. Solids **134**, 103750 (2020).
58 M. H. Joudivand Sarand, and I. B. Misirlioglu, A physics-based plasticity study of the mechanism of inhomogeneous strain evolution in dual phase 600 steel, Int. J. Plast. **174**, 103918 (2024).
59 J. C. Zhu, M. Ben Bettaieb, and F. Abed-Meraim, Investigation of the competition between void coalescence and macroscopic strain localization using the periodic homogenization multiscale scheme, J. Mech. Phys. Solids **143**, 104042 (2020).
60 J. Zhu, M. B. Bettaieb, and F. Abed-Meraim, Numerical investigation of necking in perforated sheets using the periodic homogenization approach, Int. J. Mech. Sci. **166**, 105209 (2020).
61 T. Kuwabara, R. Tachibana, Y. Takada, T. Koizumi, S. Coppieters, and F. Barlat, Effect of hydrostatic stress on the strength differential effect in low-carbon steel sheet, Int. J. Mater Form. **15**, 13 (2022).
62 R. Maeda, Z. L. Wang, T. Ogawa, and Y. Adachi, Stress-strain partitioning behavior and mechanical properties of dual-phase steel using finite element analysis, Mater. Today Commun. **25**, 101658 (2020).
63 S. Lee, H. Cho, C. A. Bronkhorst, R. Pokharel, D. W. Brown, B. Clausen, S. C. Vogel, V. Anghel, G. T. Gray Iii, and J. R. Mayeur, Deformation, dislocation evolution and the non-Schmid effect in body-centered-cubic single- and polycrystal tantalum, Int. J. Plast. **163**, 103529 (2023).

基于位错密度晶体塑性模型的双相钢非施密特效应研究

朱渐昌, Mohamed Ben Bettaieb, 李振环, Farid Abed-Meraim, 黄敏生

摘要 近年来, 体心立方(BCC)单相金属中的非施密特(NS)效应受到了广泛的关注. 然而, 对双相(DP)钢BCC相中此效应尚未形成深入理解. 本研究探讨了铁素体-马氏体双相钢中的NS效应, 其中铁素体相具有BCC晶体结构并表现出NS效应. 分析了NS应力分量对DP钢力学行为的影响, 包括应力/应变分配、塑性流动和屈服面. 本研究采用基于位错密度的晶体塑性本构模型来描述两相的力学响应, 其中NS效应仅纳入铁素体相的模型. 本文研究结果表明, 在随机取向的等轴晶微观结构中, 法向NS应力分量在拉压不对称性中起重要作用. 相比之下, 在择优取向的细长晶结构中, 晶体织构和NS效应存在明显的耦合作用. 这些发现促进了我们对微观结构特征和NS效应之间复杂相互作用的认识, 并有助于阐明DP钢各向异性-拉压不对称塑性行为的机制.